Finite Control Set Model Predictive Control of Grid Tied Wind Turbine Converter

Masters Thesis

Laurits Hastrup Andersen
Jeppe Nørgaard Jensen

Aalborg University
Department of Electronic Systems
Automation and Control Section

Department of Electronic Systems
Aalborg University
http://www.aau.dk

AALBORG UNIVERSITY
STUDENT REPORT

Title:
Finite Control Set Model Predictive Control of Grid Tied Wind Turbine Converter

Theme:
Masters Thesis

Project Period:
Spring 2023

Project Group:
CA 1031

Participant(s):
Jeppe Nørgaard Jensen
Laurits Hastrup Andersen

Supervisor(s):
Jakob Stoustrup
Søren Rusbjerg Andersen

Copies: 1

Page Numbers: 69

Date of Completion:
June 1, 2023

Abstract:

This report presents the proposal of finite control set model predictive control (FCS-MPC) for the control of the inverter switching signals of a grid tied wind turbine back-to-back converter. Primary control objectives are tracking of DC-link voltage, and power references, in the context of grid following. The controllers ability to reduce inverter switching loses is also considered. Performance is compared to a PI controller representing the industry standard. To facilitate predictive control, a model of the converter and filter dynamics is derived, and presented in state space form.
Simulation of converter, filter and grid is performed. Results does not shown meaningful performance advantages to suggest the proposed method as a viable alternative to industry standard PI control. However, the prospect of further development and improvements discussed suggest its potential.

Contents

Preface

This masters thesis was written by members of group CA 1031 under the guidance of Jakob Stoustrup and Søren Rusbjerg Andersen *(Vestas)*, during the 10th semester of the education in Control and Automation, Aalborg University in the Spring of 2023.

Aalborg University, June 2023

Laurits Hastrup Andersen
<lhan21@student.aau.dk>

Jeppe Nørgaard Jensen
<jnje16@student.aau.dk>

Summary of Abbreviations

AC	Alternating current
DC	Direct current
MPC	Model predictive control
FCS	Finite control set
THD	Total harmonic distortion
LCL	Inductor-Capacitor-Inductor filter
PWM	Pulse width modulation
VSC	Voltage source converter
KCL	Kirchhoff's current law
KVL	Kirchhoff's voltage law
PLL	Phase lock loop
SVM	Space vector modulation
PI	Proportional-Integral controller
RMS	Root mean square
FIR	Finite impulse response
FFT	Fast fourier transform
ZOH	Zero order hold

Chapter 1

Introduction

This chapter presents motivation behind the project, founded in global energy tendencies. The project description is also presented, followed by a report outline.

1.1 Motivation

Green solutions to energy production are increasingly important to secure a sustainable future, and the pursuit of good alternatives to fossil fuels is important to most. In this endeavour, wind energy has become a pillar of the modern energy solution. The Danish climate policies [1] states the goal of reducing greenhouse gas emission by 70% by 2030, and being climate neutral by 2050. In a windy and flat country with a long coastline like Denmark, wind energy will certainly play a crucial part of reaching the goals. The EU 2030 targets mentions 27% renewable energy in total energy consumption[1]. As such there is no doubt that research and development into wind energy conversion is worthwhile.

To allow wind energy to play its part, and to allow it as soon as possible, it is paramount to make it accessible and cheap. The efficiency also comes with large economical opportunities, which sparks the interest of companies and other financial stakeholders. For these reasons this project consider part of the electrical conversion of wind energy. A wind turbine converts wind energy to mechanical energy, and then to electrical energy. This electrical energy must be manipulated to match certain AC properties, to allow it to be injected into the grid. Optimisation and efficient design of this process is the centerpiece of this project.

1.2 Project Description

This projects proposes a model predictive control (MPC) approach for the control of a wind turbine converter. MPC is a suited control method for its ability do deal with non-linear systems, and ease of incorporating constraints. Furthermore well defined models exist for power systems, which lend itself well to model prediction schemes. Additionally the converter has a finite set of actuation inputs, which is utilized in the proposal by specialised version of MPC, this is called finite control set model predictive control (FCS-MPC). A wind turbine generator is decoupled from the grid by AC-DC-AC conversion, this project focuses on control of the converter responsible of the last conversion from DC back to AC. Modern electrical energy is distributed in three phase AC, controlling the converter allows individual control over each phase and its currents can be shaped to a desired wave form. A converter is non-linear by nature of its discreteness, its raw output current is square waved. To achieve a sinusoidal waveform a filter is added between converter and grid, consisting of passive power components. The intricacies of FCS-MPC, the converter and the filter, are further discussed throughout the chapters of this report.

The goal of this project is to research the viability of the FCS-MPC approach in regards to the control objectives listed below. The project considers a 4MW wind turbine.

- Reference tracking of the DC-link voltage. The turbine generator supplies a changing input current to the converter, to avoid instability in the DC-link voltage, it must be controlled to maintain a desired value. A reference value of 1000V is used.
- Reference tracking of the active- and reactive power. To maximise power production its desired to strive for unity power factor, in practise, this means reactive power should be controlled towards a steady value of zero. Arbitrary references of reactive power is also considered, for the reason that grid administrators can request reactive power.
- The electrical components are subject to damage if voltage or currents stray too far from nominal values, therefore constraints are imposed on the controller:
  1. Output converter current must stay within 5.5kA
  2. Dc-link voltage must be kept within 1050 and 950 volt.
- The converter introduces harmonics in grid currents, the combination of controller and filter must results in total harmonic distortion (THD) of less than 5%.
- The flexibility of the MPC cost function should be used to minimize switching losses during converter operation, by reducing the number of commutations between switching cycles.

Wind turbine control is subject to constraints and regulation given by grid codes, which are national regulations set by individual countries. The above objectives are extracts of grid codes, and has been chosen as a focus in this project. Any real implementation of wind turbine control should consider grid codes in their entirety.

1.3 Report outline

The rest of the report is organised as follows:

Chapter 2 presents the central ideas of wind turbines and the conversion of energy. This leads to a more detailed description of the converter topology used in this project. The chapter ends with an introduction to FCS-MPC, and the reasons for why it is a suited control approach for converter control.

Chapter 3 introduces relevant *phasor* theory, and explains the reference frames used to describe three phase properties. A model for the converter and filter is derived. This is required for predictive control, and it is discretized for digital use. Filter dynamics are modelled in terms of currents and voltages, and presented in state space form.

Chapter 4 gives further details into the principal workings of FCS-MPC. Then the individual elements of the controller is described in detail in their dedicated sections.

Chapter 5 is an auxiliary chapter which clearly shows the Simulink setup used for simulation.

Chapter 6 presents simulation results. The project goals are tested and their fulfilment is analysed. FCS-MPC performance is evaluated and strengths and weaknesses are identified.

Chapter 7 discusses the findings from results, and other ideas. Further work, and project limitations are discussed.

Chapter 8 concludes the project, its goals are evaluated. And final remarks are made on the results of the project.

Chapter 2

Wind turbines, Converters and MPC

This chapter presents an overview of the energy production in a wind turbine, to show the context of the focus of this report, the converter. Converter topology is then explained, followed by an introduction to MPC. Lastly the reasoning for a converter filter is described.

2.1 The Wind Turbine and Energy Conversion

The energy output of a wind turbine relies on its ability to convert kinetic wind energy into electrical energy. This conversion process, and a wind turbine in general is usually split into two distinct areas, the mechanical side and the electrical side.

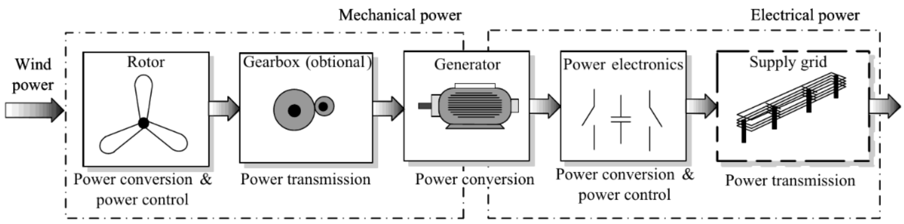

Figure 2.1: Energy conversion of a wind turbine [2].

Fig. 2.1 shows a simple diagram of the primary elements of each side. The central element is a generator which convert mechanical rotation into electrical alternating current. Modern implementations of the mechanical side requires comprehensive control design to efficiently and safely extract the wind energy. Although many elements and operation of each side is interlinked, the system can be simplified by decoupling the generator from the grid. Current converter topologies does this in a back-to-back manner, by converting the generator AC current to DC current and immediately converting back to AC current. Previous wind turbines did not do this and required a gearbox between rotor and generator to maintain an adequate generator frequency compared to the static grid frequency. Modern turbines are variable-speed turbines through the decoupling, meaning the mechanical side control is free to maximize power production based on wind conditions independently of grid conditions.

2.2 The Back-to-Back converter

Besides decoupling, the main advantage of this converter topology is the ability to control the active and reactive power injected into the grid. This in turn can contribute to limit the effects of grid faults and to the stabilisation of grid voltage or frequency, restoring normal operation after a fault. As a remark, note that the control of power is performed by controlling the phase angle between converter output current, and grid voltage. The power controller produces the desired phase angle by setting appropriate current references to a current controller, which ultimately controls the converter switching.

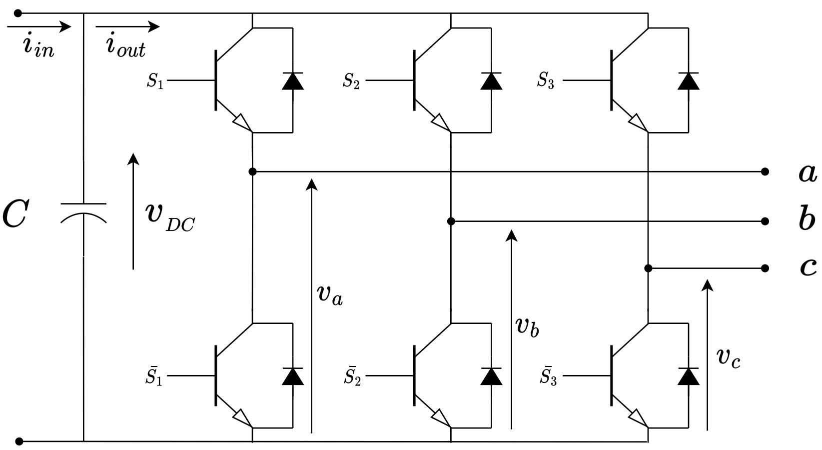

Figure 2.2: 2-level voltage source inverter.

Fig. 2.2 shows the simple, but widely used, converter topology used in this project. Notice that only the inverter side of the back-to-back converter is shown, throughout this project the converter rectifier and the mechanical side generator is disregarded and implementation of the DC input i_{in} to the inverter is not considered. It is assumed that the input current can be represented by a steady DC current. The voltage source inverter is characterized by a capacitor placed at the DC-link, its purpose is both filtering and storage ensuring a smooth and controllable DC-link voltage v_{DC}. The AC properties of each phase a, b and c are created by controlling a three-phase bridge consisting of six switches with a free-wheeling diode to allow negative reactive power flow. The switches are controlled by switching signal $S = [S_1 S_2 S_3]$. The upper and lower leg of a phase can never be closed simultaneously to avoid short circuit, therefore the lower legs are controlled by the boolean opposite of the switching signals denoted by a bar $\bar{S_1}$. Based on the switching signal S, a single phase, or a combination of two may be connected to the DC-link applying its voltage v_{DC} to the phase or phases. The resulting current depends on the state of the remaining circuit including the grid and possibly a filter, these are either measured or modelled, which combined allows prediction of the resulting phase currents. It is these predictions which are used in the control scheme to select desired switching signals.

A 2-level converter is able to output two voltage levels, 0 and v_{DC}. The discrete nature of switching between these values means the natural output of the converter is a square wave, which very poorly matches the sinusoidal signals of the grid. The solution is to implement fast switching in the form of pulse width modulation (PWM) combined with an inductor. The charging and discharging of the inductor between switching cycles acts as a low-pass filter resulting in a smooth signal, much more compatible with the grid. The remaining ripples are called harmonic disturbance and must not exceed some threshold given by grid codes, reduction of harmonic distortion can be improved via additional filtering e.g. *inductor-capasitor-inductor* (LCL) filter. However, more filtering comes at the expense of increased losses. The inductor filter is extended to a LCL filter in most wind turbine applications, this allows good filtering while avoiding very large passive component values, which is important to reduce physical size and cost. The improvements comes at the cost of filter complexity, the filter constitute the governing dynamics of the converter and are discussed in Chapter 3.

2.3 Grid Filter

The use of a converter and the forced discrete control of it, inherently creates harmonics in the output. Harmonics disturb sensitive equipment, and increases losses, therefore a grid filter removing them is necessary. The simplest solution is to place an inductor between the converter and the grid. However, the nature of wind turbines with high power and low switching frequency, means a very large inductor value is required, which is both expensive and cumbersome for its size. Grid codes typically require compliance with limitations that take place for frequencies above a threshold. As such the common solution is LCL filter providing low-pass filter attenuation, the combination of inductors and capacitor allows use of components with much smaller values. The passive components of the filter yield smoothing of the AC current by charging/discharging between switching cycles. These components also dictate the converter dynamics, meaning the overall converter design becomes a trade-off between fast dynamics and high filtering [2]. The filter performance is reflected in the total harmonic distortion (THD) of the *converter-filter* current output injected into the grid.

Filter design is an important part of the converter, but not within the scope of this project. The filter used in this project is a generic LCL filter supplied by Vestas.

2.4 Model Predictive Control of Converter

This section presents the reasons that converter control lend itself well to MPC. The essence of predictive control is the use of a model to predict its future states, accurate models are therefore crucial to MPC performance. Power electronic components are well known and their dynamics can be modelled easily and precisely, allowing good predictions. The multiple objectives of converter control in a wind turbine context are also easily handled in MPC, where all objectives are gathered in a cost function. The cost function terms are weighted, and can be designed to reflect the desired priority of each objective. A drawback of MPC is its computational effort, optimal actuation is selected based on minimizing the cost function using predicted states. This is often very demanding, and requires significant computation time. However, the three-phase 2-level converter mentioned above with its six switches, only has eight distinct switching states. This finite number of possible actuations can be utilized to simplify the optimization process to achieve a greatly reduced computational requirement compared to the usual continuous optimisation. Finally, a converter has several hard constraints to guarantee correct operation and avoid damaging components. In MPC, any actuation resulting in a violation of these constraints can be assigned a high cost, meaning constraints can be easily managed in a flexible manner. These concepts and more are further discussed in Chapter 4.

Chapter 3

Modelling

This chapter derives a model of the system. The converter is considered first, followed by some relevant theory on reference frames. Then the filter dynamics are described in a state space form, and discretised.

3.1 Phasors

By the nature of alternating current, both voltages and current are expressed in terms of sinusoid waves. The analysis of oscillating systems are often simplified by using phasors, which allow a more compact description of sinusoids in the complex domain. A sinusoidal function is defined:

$$f(t) = Acos(\omega t + \theta) \tag{3.1}$$

where A is the maximum amplitude, ω is the angular frequency, and θ is the phase shift.

Including an imaginary component, allows the use of Eulers identity, which relates sinusodial waves to the complex domain:

$$Acos(\omega t + \theta) + jAsin(\omega t + \theta) = Ae^{j(\omega t + \theta)} \tag{3.2}$$

where j is the complex operator, and the right side is a phasor. Notice that a phasor is comprised of the amplitude and two rotations, the varying rotation depending on angular frequency, and a constant rotation given by the phase shift. The original sinusoidal $f(t)$ is clearly equivalent to the real part of the phasor.

Lets consider the instantaneous relationship for which the varying rotation from ω is disregarded, and we instead look at how the instantaneous position of a phasor, leads to the correct sinusoidal values.

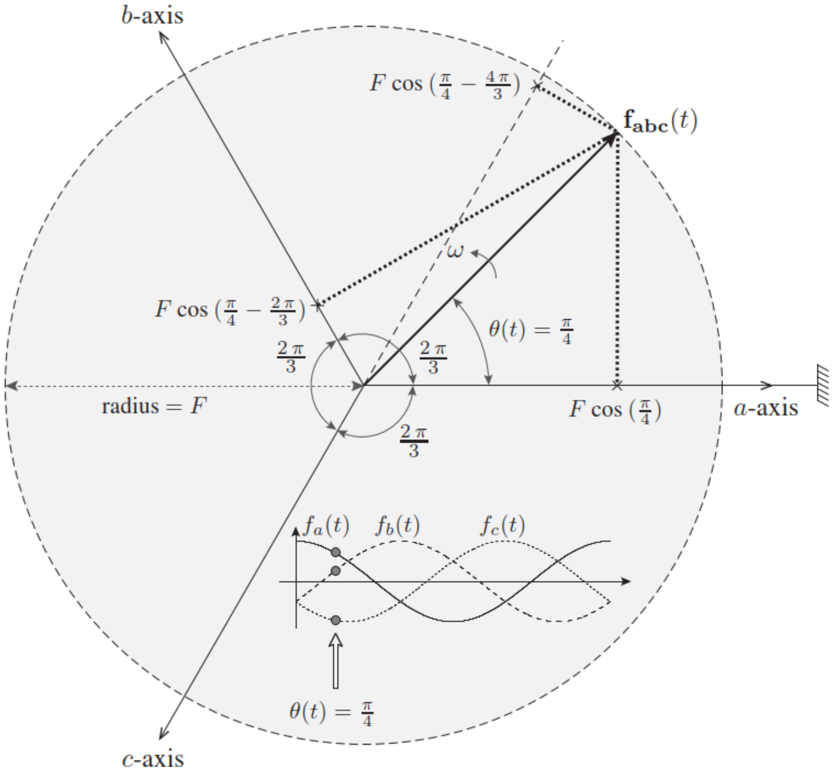

Figure 3.1: Phasor angle to sinosodial values [3].

Fig. 3.1 shows the individual three phase sinusoidal f_a, f_b and f_c given by Eq. (3.1) represented by three axes rotated by 120° and f_a being the reference axis. A phasor f_{abc} rotating with angular frequency ω in the frame denoted by these three axes can represent the three functions by its projection onto the axes. The following equation shows how the phasor position can be computed when given a set of values for the three sinusoids.

$$f_{abc} = \frac{2}{3}(f_a + \mathbf{a} f_b + \mathbf{a}^2 f_c) \tag{3.3}$$

Where $\mathbf{a} = e^{j\frac{2\pi}{3}}$ is equivalent to a 120° rotation which is the natural phase shift between a three phase ac signal. The fraction 2/3 is necessary to maintain correct length A of the phasor. Adding the three sinusoidal values and multiplying by 2/3 will always yield the maximum amplitude A of the three waves assuming they have equal maximum amplitude. Using Eq. (3.3) the individual values of f_a, f_b and f_c can be isolated and computed for a given phasor.

If we instead look at the rectangular rotation instead of an angle $\mathbf{a} = e^{j\frac{2\pi}{3}} = -\frac{1}{2} + j\frac{\sqrt(3)}{2}$, we get the phasor represented in terms of the two stationary axis α and β which are aligned with the real and complex axis, see Fig. 3.2. Defining phasors in the *alfa-beta* domain is common practice in electronic engineering for the simplicity in describing three variables with just two variables.

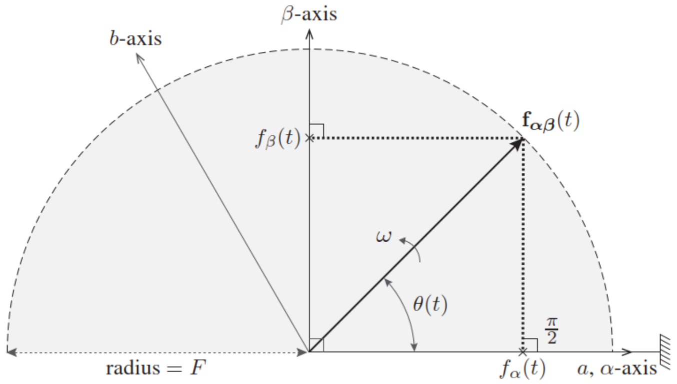

Figure 3.2: Phasor represented in $\alpha - \beta$ domain [3].

The transformation from the natural frame of a, b and c into the stationary $\alpha - \beta$ frame is known as the Clarke transformation. The Clark transformation can include a 0-phase element, which is related to transformation of unbalanced three-phase systems. This project assumes balanced systems and the 0-phase element is redundant. The Clark transformation without 0-phase, is defined by the matrix relationship [4]:

$$\begin{bmatrix} f_\alpha \\ f_\beta \end{bmatrix} = \frac{2}{3} \begin{bmatrix} 1 & -\frac{1}{2} & -\frac{1}{2} \\ 0 & \frac{\sqrt{(3)}}{2} & -\frac{\sqrt{(3)}}{2} \end{bmatrix} \begin{bmatrix} f_a \\ f_b \\ f_c \end{bmatrix} \tag{3.4}$$

and the equivalent instantaneous vector $\mathbf{f}_{\alpha\beta}$ is given by:

$$\mathbf{f}_{\alpha\beta} = f_\alpha + j f_\beta \tag{3.5}$$

Note that such a vector exist for both current $(i_{\alpha\beta})$ and voltage $(v_{\alpha\beta})$.

3.2 Converter Model

This section derives a model for the output voltage of the 2-level voltage source converter (VSC), shown on figure 3.3. The aim is to describe the voltage in the $\alpha\beta$ domain in terms of voltage vectors. Since the output does not have any oscillating properties, the vectors will correspond to the instantaneous position of a phasor as mentioned in the previous section.

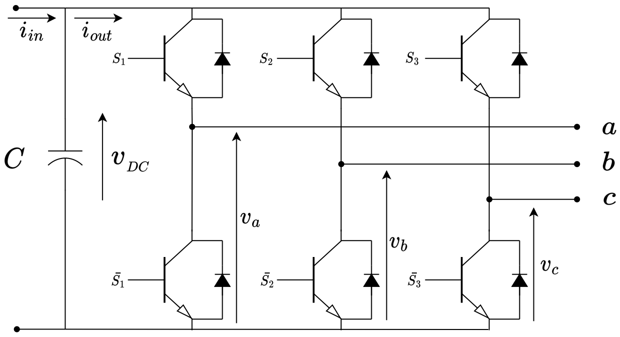

Figure 3.3: 2 level voltage source converter.

The switching function related to each phase is denoted S_x, with $x = a, b, c$ and is defined by the complementary relationship shown below:

$$S_a = \begin{cases} 1 & \text{if } S_1 = 1 \text{ and } \bar{S_1} = 0 \\ 0 & \text{if } S_1 = 0 \text{ and } \bar{S_1} = 1 \end{cases} \tag{3.6}$$

$$S_b = \begin{cases} 1 & \text{if } S_2 = 1 \text{ and } \bar{S_2} = 0 \\ 0 & \text{if } S_2 = 0 \text{ and } \bar{S_2} = 1 \end{cases} \tag{3.7}$$

$$S_c = \begin{cases} 1 & \text{if } S_3 = 1 \text{ and } \bar{S_3} = 0 \\ 0 & \text{if } S_3 = 0 \text{ and } \bar{S_3} = 1 \end{cases} \tag{3.8}$$

The output voltage for each phase can now be calculated from the DC-link voltage v_{DC}, by the switching function as follows:

$$v_x = S_x v_{DC} \tag{3.9}$$

Having the corresponding voltage on each phase associated with a switching function, we can produce the voltage vector in accordance with Eq. (3.3)[5]:

$$\mathbf{V} = \frac{2}{3}(v_a + \mathbf{a}v_b + \mathbf{a}^2 v_c) \tag{3.10}$$

where once again $\mathbf{a} = -\frac{1}{2} + j\frac{\sqrt{(3)}}{2}$. With three switching states, each with two outcomes, the combination of switching states can take $2^3 = 8$ unique values depending on the combination of S_a, S_b and S_c. There are therefore also eight corresponding voltage vectors $\mathbf{V}$. There are however only seven unique values for $\mathbf{V}$ as shown in table 3.1, as $\mathbf{V}_0 = \mathbf{V}_7 = 0$.

S_a	S_b	S_c	$\mathbf{V}$
0	0	0	$\mathbf{V}_0 = 0$
1	0	0	$\mathbf{V}_1 = \frac{2}{3}v_{DC}$
1	1	0	$\mathbf{V}_2 = \frac{1}{3}v_{DC} + j\frac{\sqrt{3}}{3}v_{DC}$
0	1	0	$\mathbf{V}_3 = -\frac{1}{3}v_{DC} + j\frac{\sqrt{3}}{3}v_{DC}$
0	1	1	$\mathbf{V}_4 = -\frac{2}{3}v_{DC}$
0	0	1	$\mathbf{V}_5 = -\frac{1}{3}v_{DC} - j\frac{\sqrt{3}}{3}v_{DC}$
1	0	1	$\mathbf{V}_6 = \frac{1}{3}v_{DC} - j\frac{\sqrt{3}}{3}v_{DC}$
1	1	1	$\mathbf{V}_7 = 0$

Table 3.1: Value of the voltage vector, given the switching states.

These voltage vectors in the complex domain are linked to the $\alpha\beta$ domain in the sense that the real part correspond to α and the imaginary part correspond to β. The rest of the model is also derived in the $\alpha\beta$ domain, and allows direct interaction with these voltage vectors. Note that this model is very simple assuming an ideal converter, a more accurate model might include dead time and other more complex features of a converter [5]. For the scope of this report the simple model is deemed sufficient.

3.3 Filter Model

Having the voltage output form the converter, the filter between the converter and grid is considered to model the resulting current dynamics. A simple inductor filter is considered first to establish a foundation, then the widely used LCL filter is considered by the inclusion of an additional inductor and a capacitor.

3.3.1 RL Filter

The fundamental operation of the converter relies on some filtering between the discrete output voltage and the sinusoidal grid. Using an inductor can achieve the necessary low-pass filtering on the voltage output, but requires large inductor values.

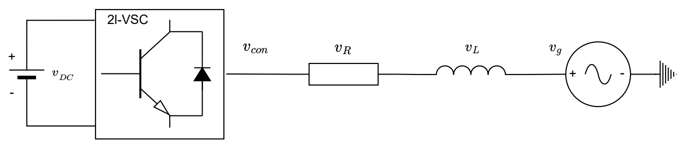

Figure 3.4: RL filter circuit

An inductor is a coil of wire wound around a core, a current flowing through the wire creates a magnetic field. This field builds or collapses according to the current flowing through the coil, the self induced energy stored in the field creates an opposing effect to current changes. When current flow is decreasing, the field collapses, releasing energy into the circuit, maintaining current flow for a short duration. According to Faraday's law the electromotive force (voltage) induced by a change of flux is:

$$\varepsilon = -\frac{d\Phi}{dt} \tag{3.11}$$

where the change of magnetic flux Φ through a coil is given by:

$$\frac{d\Phi}{dt} = u_0 n^2 l A \frac{di}{dt} = L\frac{di}{dt} \tag{3.12}$$

where u_0 is the magnetic constant, n is the wire turns per length, l is the coil length and A is its cross sectional area, these coil constants define the inductance L of an inductor. The negative sign in Eq. (3.11) is given by Lenz's law, stating that the induced voltage of an inductor behaves such that it opposes a current change. By convention of circuit theory, the plus and minus direction of the inductor is such that a voltage opposing negative current change is also negative, therefore when using Eq. (3.11) to compute the self induced voltage we have:

$$v_L = L\frac{di}{dt} \tag{3.13}$$

Fig. 3.5 shows the RL circuit schematic for a single phase while letting the converter function as a voltage source.

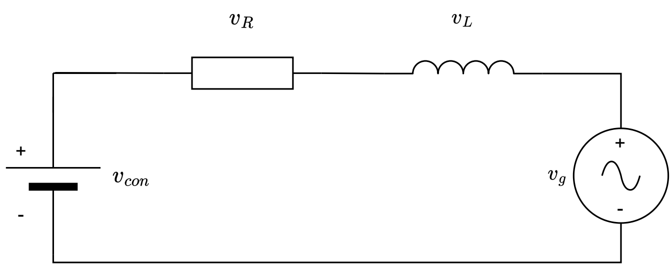

Figure 3.5: RL filter circuit with converter acting as a voltage source.

The current dynamics can be computed based on Kirchhoff's voltage law:

$$v_{con} - v_R - v_L - v_g = 0 \tag{3.14}$$

where v_{con} is equivalent to the voltage of a single phase v_x Eq. (3.9). Inserting Eq. (3.13) and using the Ohm's law for v_R:

$$v_{con} - Ri - L\frac{di}{dt} - v_g = 0 \quad \Rightarrow \quad \frac{di}{dt} = -\frac{R}{L}i + \frac{v_{con}}{L} - \frac{v_g}{L} \tag{3.15}$$

We now have the dynamics of the current given by the measured variables i and v_g and the input v_{con}.

3.3.2 LCL Filter

The LCL filter is modelled by similar approach, but is more complicated. The addition of a capacitor adds opposition to voltage changes. A capacitor builds up electrons when connected to a voltage source, current flows through the capacitor until the electrons charge equal the source. If the source changes, the capacitor releases electrons in an attempt to maintain the initial voltage. As such, the relationship between current and voltage is:

$$i = C\frac{dv}{dt} \tag{3.16}$$

The LCL filter circuit is:

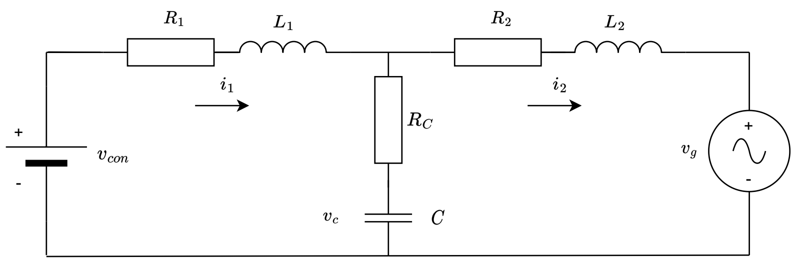

Figure 3.6: RLC filter circuit with converter acting as a voltage source.

The states of interest are $x = [i_1 \;\; i_2 \;\; v_c]^T$. The state vector contains the converter current which is under direct control, the grid current which appears in the dynamics of the other variables, and the filter capacitor voltage.

The dynamics of all states can be found using KVL and KCL:

$$\begin{aligned}
&\text{KVL Left loop:} && -v_{con} + R_1 i_1 + L_1\frac{di_1}{dt} + R_c(i_1 - i_2) + v_c = 0 \\
&\text{KVL Right loop:} && -v_c - R_c(i_1 - i_2) + R_2 i_2 + L_2\frac{di_2}{dt} + v_g = 0 \\
&\text{KCL for } i_C\text{:} && i_1 - i_2 - i_C = 0 \quad \Rightarrow \quad i_1 - i_2 = i_C = C\frac{dv_c}{dt}
\end{aligned} \tag{3.17}$$

Rewriting to isolate dynamics of state variables:

$$
\begin{aligned}
\frac{di_1}{dt} &= \frac{v_{con}}{L_1} - \frac{R_1 + R_c}{L_1} i_1 + \frac{R_c}{L_1} i_2 - \frac{1}{L_1} v_c \\
\frac{di_2}{dt} &= \frac{1}{L_2} v_c + \frac{R_c}{L_2} i_1 - \frac{R_2 + R_c}{L_2} i_2 - \frac{1}{L_2} v_g \\
\frac{dv_c}{dt} &= \frac{1}{C} i_1 - \frac{1}{C} i_2
\end{aligned}
\tag{3.18}
$$

The dynamics in state space representation are:

$$
\dot{x} = Ax + B_1 u + B_2 v_g \tag{3.19}
$$

where $u = v_{con}$ is the input voltage and the relationship to v_g is modelled as an additional input. Expanding the state vector and inputs to contain the $\alpha\beta$ components of each variable:

$$
x = \begin{bmatrix} i_{1\alpha} & i_{1\beta} & i_{2\alpha} & i_{2\beta} & v_{c\alpha} & v_{c\beta} \end{bmatrix}^T \qquad u = \begin{bmatrix} v_{con\alpha} & v_{con\beta} \end{bmatrix}^T \qquad v_g = \begin{bmatrix} v_{g\alpha} & v_{g\beta} \end{bmatrix}^T
$$

$$
\dot{x} = \begin{bmatrix}
\frac{-(R_1+R_c)}{L_1} & 0 & \frac{R_c}{L_1} & 0 & \frac{-1}{L_1} & 0 \\
0 & \frac{-(R_1+R_c)}{L_1} & 0 & \frac{R_c}{L_1} & 0 & \frac{-1}{L_1} \\
\frac{R_c}{L_2} & 0 & \frac{-(R_1+R_c)}{L_2} & 0 & \frac{1}{L_2} & 0 \\
0 & \frac{R_c}{L_2} & 0 & \frac{-(R_1+R_c)}{L_2} & 0 & \frac{1}{L_2} \\
\frac{1}{C_f} & 0 & \frac{-1}{C_f} & 0 & 0 & 0 \\
0 & \frac{1}{C_f} & 0 & \frac{-1}{C_f} & 0 & 0
\end{bmatrix} x + \begin{bmatrix}
\frac{1}{L_1} & 0 \\
0 & \frac{1}{L_1} \\
0 & 0 \\
0 & 0 \\
0 & 0 \\
0 & 0
\end{bmatrix} u + \begin{bmatrix}
0 & 0 \\
0 & 0 \\
\frac{-1}{L_2} & 0 \\
0 & \frac{-1}{L_2} \\
0 & 0 \\
0 & 0
\end{bmatrix} v_g
\tag{3.20}
$$

The continuous model is discretized to be compatible with digital control. For simplicity the forward Euler method is used in this project. Consider the following approximation of a change of variable over a sample time T_s between the current sample k and the next $(k+1)$ with equivalent time of kT_s and $(kT_s + T_s)$ respectively:

$$
\left\{ \frac{dx(t)}{dt} \right\}_{t=kT_s} \approx \frac{x(kT_s + T_s) - x(kT_s)}{T_s} \tag{3.21}
$$

Then isolating the next sample:

$$
x(kT_s + T_s) \approx x(kT_s) + T_s \left\{ \frac{dx(t)}{dt} \right\}_{t=kT_s} \tag{3.22}
$$

The differential term is given by Eq. (3.19), when inserted the discretisation becomes:

$$\begin{aligned} x(kT_s + T_s) &\approx x(kT_s) + T_s\Big(Ax(kT_s) + B_1u(kT_s) + B_2v_g(kT_s)\Big) \\ &\approx (I + T_sA)x(kT_s) + T_sB_1u(kT_s) + T_sB_2v_g(kT_s) \end{aligned} \tag{3.23}$$

The use of forward Euler is a simple discretisation method, which will introduce some discretisation error, the use of an exact discretisation method is discussed in Chapter 7.

3.3.3 DC-link Model

The state space is augmented with an additional state V_{DC} which is used to check for constraint violation. The model is not immediately easy to derive, since the state is single phase DC, and the remaining states are three phase AC. However, one property is constant across the converter, the power going in and out is equal, assuming ideal converter. The following equations relate to Fig. 3.3, the DC-link capacitor voltage can be achieved by:

$$P_{in} = P_{out} \quad \rightarrow \quad v_{DC}I_{out} = v_{1\alpha}i_{1\alpha} + v_{1\beta}i_{1\beta} \tag{3.24}$$

by KCL the DC-link output current is given by:

$$i_{out} = i_{in} - i_{DC} = i_{in} - C_{DC}\frac{dv_{DC}}{dt} \tag{3.25}$$

by inserting Eq. (3.25) into Eq. (3.24) the capacitor voltage dynamics are obtained:

$$\begin{aligned} v_{DC}\left(i_{in} - C_{DC}\frac{dv_{DC}}{dt}\right) &= v_{1\alpha}i_{1\alpha} + v_{1\beta}i_{1\beta} \\ i_{in} - C_{DC}\frac{dv_{DC}}{dt} &= \frac{v_{1\alpha}i_{1\alpha} + v_{1\beta}i_{1\beta}}{v_{DC}} \\ -C_{DC}\frac{dv_{DC}}{dt} &= \frac{v_{1\alpha}i_{1\alpha} + v_{1\beta}i_{1\beta}}{v_{DC}} - i_{in} \\ \frac{dv_{DC}}{dt} &= -\frac{\frac{v_{1\alpha}i_{1\alpha}+v_{1\beta}i_{1\beta}}{v_{DC}} + i_{in}}{C_{DC}} \end{aligned} \tag{3.26}$$

This is discretised in the same manner as previously.

Chapter 4

FCS-MPC

This chapter presents finite control set model predictive control (FCS-MPC). The brief introduction in Chapter 2 is expanded upon, and additional concepts are introduced. Then the individual parts of the controller is described in detail.

4.1 Principal Concept of FCS-MPC

Because the combinations of converter switching states only results in eight distinct options, the control input is said to be a finite control set, e.g. consisting of the eight voltage vectors $\mathbf{V}_0 ... \mathbf{V}_7$. The availability of a finite control set allows the control algorithm to perform much simpler optimisation compared to standard MPC. The basic idea of standard MPC are: using a model to predict future behaviour based on different inputs, assigning each input a cost by comparing predictions to desired behaviour in a cost function, obtain optimal actuation based on minimising cost. One of the primary advantages is that the current actuation input, can be optimised based on its impact on the future. This is done by optimising over a finite length horizon, from which a set of optimised actuation inputs for each time step is obtained, the first input of the set is then applied. Then the entire horizon is moved forward by one step and repeated.

Optimisation is a demanding process, the computation time is often irrelevant in control problems, but the relatively quick oscillations of 50Hz AC means even a short delay results in outdated measurements. The system dynamics are fast enough that the time it takes to find an optimised actuation and be ready to apply it, can be long enough that the measurement used for optimisation will be outdated. As such the emphasis on a fast control algorithm is increased, for which the finite control set is a great advantage. A small number of inputs allow a brute-force approach to optimisation, where predictions and their cost can be computed directly for each input, and the input with lowest cost can be selected directly. This approach does, however, rely on a short horizon to be effective as the scope of brute-forcing increases drastically with the number of predictions. The number of computations are given by u^h, where u is the number of predictions, and h is the length of the horizon.

For these reasons the FSC-MPC approach to converter control often use a very short horizon with length 1 or 2 [5, 6]. Where length of two is primarily included to compensate for the delay introduced even by such a short horizon.

The implications of being limited to a short horizon means the advantage of knowing the future impact of actuations is limited, in some cases an actuation may results in optimal performance in the near future, but begin a trajectory resulting in poor future performance. An example is the optimal selection of actuations near constraints, for which the short sighted optimal actuation can result in future unavoidable violation of constraints. The computational burden of any MPC scheme is heavily decided by the lengths of the prediction and control horizon. For which different options are discussed in Chapter 7.

The remainder of this chapter describes the different blocks in the control structure seen on figure 4.1. Including prediction and cost function already mentioned in Chapter 1, and the two new elements: reference generation and extrapolation of references.

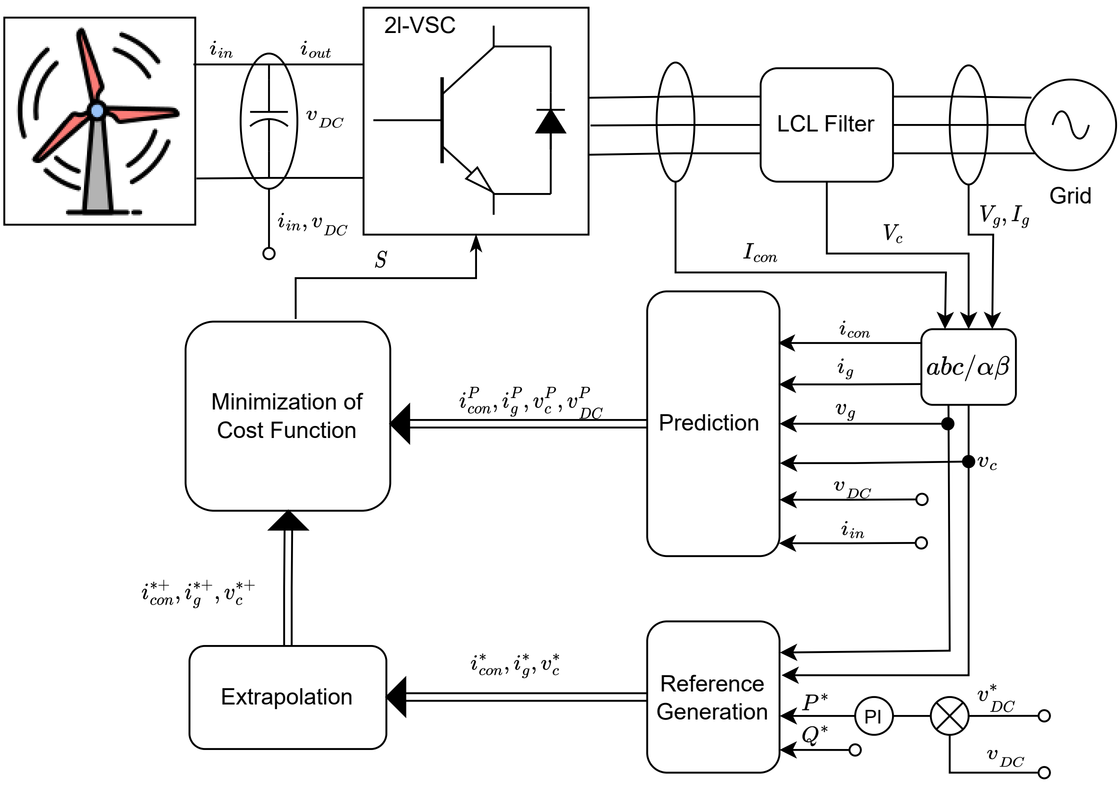

Figure 4.1: Block diagram describing the elements of FCS-MPC and the relationship between them.

4.2 Prediction

The *Prediction* block calculates the eight different current predictions using the model found in Chapter 3, given the eight voltage vectors, the equations of statespace Eq. (3.20) are computed yielding $\alpha\beta$ predictions for each vector. Note that all the states and the grid voltage are measured and converted to the $\alpha\beta$-domain before calculation.

With a prediction horizon of one, nothing more happens here. However, for longer horizons new prediction are made based on the first prediction and so on.

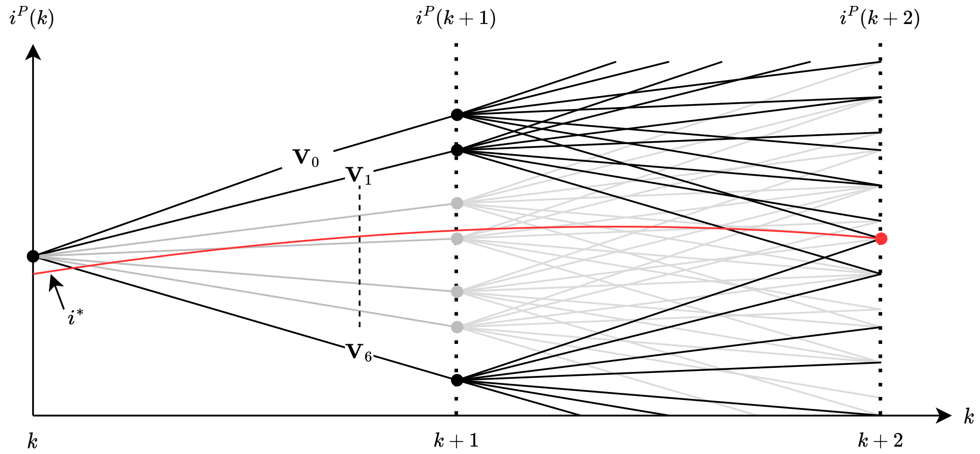

Figure 4.2: Prediction for each voltage vector for a horizon of two. Red line indicates a reference current.

Fig. 4.2 visualise how the brute-force approach escalates for longer horizons. A red line indicating a arbitrary reference current is included to show how the individual trajectories can be compared to a reference. Both in standard- and FCS-MPC a method to reduce the computational effort of long horizons is to shorten the control horizon. The control horizon is shorter than the prediction horizon, and marks a sample point from which the control is no longer optimized, but kept constant. This reduces the computational burden of computing the remaining prediction horizon.

Fig. 4.3 shows the same prediction, but with a control horizon of one. The nature of this method has the additional benefit of favouring trajectories with less switching commutations, which yield reduced losses [3]. This project focuses on prediction horizon of two, with control horizon of one, but will make comparisons to longer horizons.

4.2.1 Delay Compensation

Although FCS-MPC greatly reduced the computational burden of the control scheme compared to regular MPC, a large number of calculations are still required. This introduced a considerable delay between measurement and actuation, which reduces performance. This

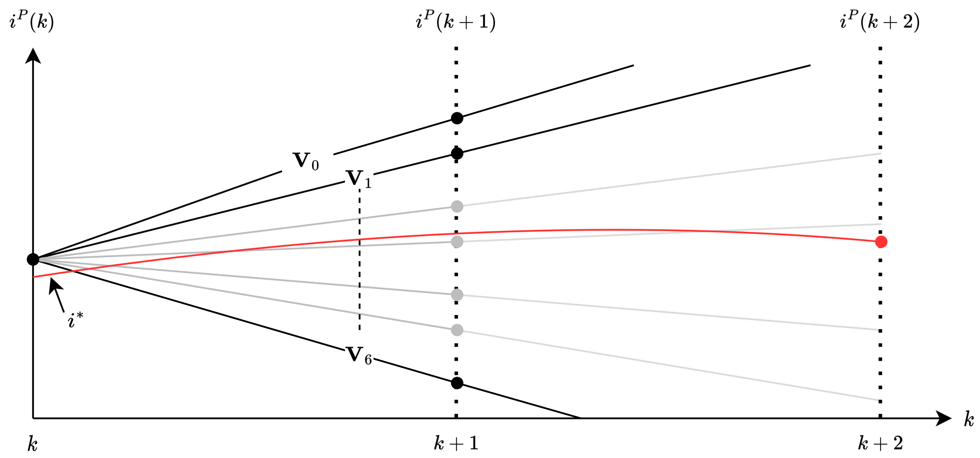

Figure 4.3: Prediction for each voltage vector for a horizon of two. With a control horizon of one.

is rarely an issue in MPC applications since the delay due to calculation time is negligible compared to most system dynamics. However, the combination of fast oscillations from 50Hz ac and no modulation, means the MPC operates on a timescale of 20kHz. At such fast sampling there is a significant delay from measurements are taken until the optimal actuation is computed and ready, meaning the predicted value is not reached before the next sampling time Fig. 4.4.

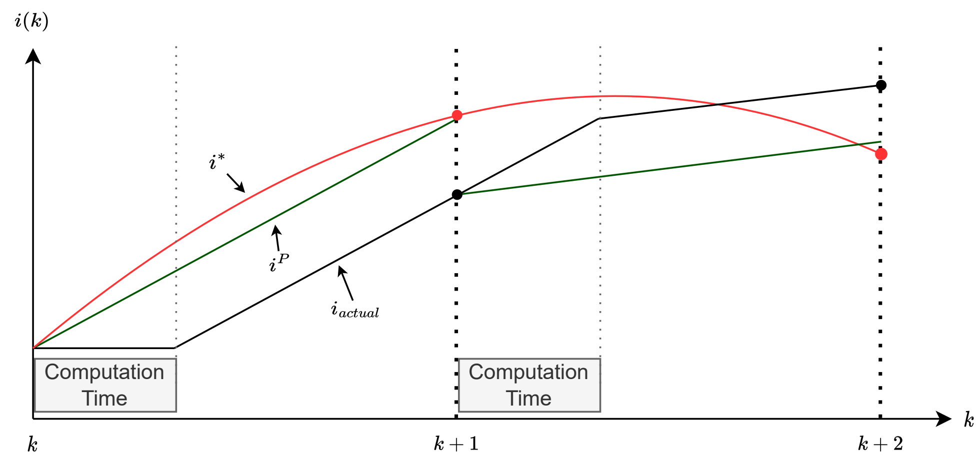

Figure 4.4: Visualisation of how prediction are never achieved without delay compensation. Red is reference, green is predicted trajectory based on selected optimal actuation, black is actual trajectory. MPC delay length is shown by the grey box.

The delay can be compensated by prediction $(k+2)$ samples ahead by the methods above, and calculating corresponding future references. By adding a one-sample delay to the application of the optimised actuation input we are purposely looking for the optimised input at $k+1$. As such the current k'th input, is computed by the previous sample. The FCS-MPC scheme essentially operates in the future, meaning at every sampling step the optimal actuation is always ready. This method assumes the computation induced delay is shorter than one sample time.

Note that delay compensations is not a natural occurring issue in Simulink, since the simulation pauses during computation time, essentially yielding 0 delay. Therefore a one-sample delay is added to simulate the effect of real world implementation.

4.3 Reference Generation

Current references are generated based on active and reactive power demands. These powers can be expressed as complex power [4]:

$$S = \mathbf{V}\bar{\mathbf{I}} = (V\angle\theta_V)(I\angle-\theta_I) = \underbrace{VIcos(\theta_V-\theta_I)}_{\text{P}} + \underbrace{jVIsin(\theta_V-\theta_I)}_{\text{Q}} \tag{4.1}$$

where $\mathbf{V}$ and $\mathbf{I}$ are phasors, $\bar{\mathbf{I}}$ indicates complex conjugate of I, and the active (P) and reactive (Q) power components are clearly apparent by definitions:

$$P = VIcos(\phi) \qquad\qquad Q = VIsin(\phi) \tag{4.2}$$

where ϕ is a phase and here correspond to $(\theta_V - \theta_I)$.

The complex conjugate $\bar{\mathbf{I}}$ is necessary to be coherent with convention that reactive power is positive for inductive loads i.e. current lags voltage such that $\theta_V > \theta_I$.

The phasor representation of V and I implies they are only correct for fixed frequency and in steady state. Using the instantaneous voltage and current vectors in the $\alpha\beta$-domain Eq. (3.5), we can define instantaneous complex power [4]:

$$S = v_{\alpha\beta}\bar{i}_{\alpha\beta} = (v_\alpha + jv_\beta)(i_\alpha - ji_\beta) = \underbrace{(v_\alpha i_\alpha + v_\beta i_\beta)}_{\text{P}} + \underbrace{j(v_\beta i_\alpha - v_\alpha i_\beta)}_{\text{Q}} \tag{4.3}$$

Writing active and reactive power in terms of voltage and current in the $\alpha\beta$-domain:

$$\begin{bmatrix} P \\ Q \end{bmatrix} = \begin{bmatrix} v_\alpha & v_\beta \\ v_\beta & -v_\alpha \end{bmatrix} \begin{bmatrix} i_\alpha \\ i_\beta \end{bmatrix} \tag{4.4}$$

Rewriting Eq. (4.4) the $\alpha\beta$ currents are now described as functions of voltages and powers P and Q.

$$\begin{bmatrix} i_\alpha \\ i_\beta \end{bmatrix} = \begin{bmatrix} v_\alpha & v_\beta \\ v_\beta & -v_\alpha \end{bmatrix}^{-1} \begin{bmatrix} P \\ Q \end{bmatrix} = \frac{1}{v_\alpha^2 + v_\beta^2} \begin{bmatrix} v_\alpha & v_\beta \\ v_\beta & -v_\alpha \end{bmatrix} \begin{bmatrix} P \\ Q \end{bmatrix} \tag{4.5}$$

Given active and reactive power references and measured grid voltages, the grid current references may be computed:

$$\begin{bmatrix} i_{g\alpha}^*(k) \\ i_{g\beta}^*(k) \end{bmatrix} = \frac{1}{v_{g\alpha}^2(k) + v_{g\beta}^2(k)} \begin{bmatrix} v_{g\alpha}(k) & v_{g\beta}(k) \\ v_{g\beta}(k) & -v_{g\alpha}(k) \end{bmatrix} \begin{bmatrix} P^*(k) \\ Q^*(k) \end{bmatrix} \tag{4.6}$$

Current predictions are made for the $k+2$ iteration, which obviously creates an inaccuracy when compared to the reference. The next section shows how the references can be extrapolated to match. Many implementations with prediction horizon of one also use the assumption $\boldsymbol{i}_g^*(k) \approx \boldsymbol{i}_g^*(k+1)$, which is accurate as long as the sampling frequency is much higher than the grid frequency, resulting in very small changes of v_g between samples k and $k+1$. Due to the extra prediction from delay compensation, extrapolation is included in this project.

Eq. (4.6) states the grid current reference given in terms of the power references and grid voltage, the corresponding converter current reference $\boldsymbol{i}_{con}^*$ and the filter capacitor reference v_c^* are computed from the grid current reference. This is done because the state space model Eq. (3.20) only directly yield a converter current i_{con} for a given input voltage vector **V**. The following equations derive the computation which are based on Fig. 3.6, the voltage over the capacitor branch is given by KVL:

$$v_{R_C C}^*(k) = v_g(k) + i_g^*(k)(R_2 + L_2) \tag{4.7}$$

The voltage over the capacitor can be computed by considering the branch as a voltage divider, this yields:

$$v_C^*(k) = \frac{v_{R_C C}(k)}{1 + sCR_C} \tag{4.8}$$

where $s = j\omega$. Assuming a no-fault condition yielding constant grid frequency of $f_g =$ 50Hz, and while using $\alpha\beta$ values, s simplifies to $s = 2\pi f_g$. To accommodate faulty conditions with changing grid frequencies, a PLL circuit must be included, to detect the actual frequency.

The converter current reference can be computed by KCL:

$$i^*_{con}(k) = i^*_g(k) + i_{R_C C}(k) = i^*_g(k) + C\frac{\Delta v_c}{T_s} \tag{4.9}$$

Having the converter current reference, means a predicted converter current of a given voltage vector can be directly evaluated to the reference. The change of capacitor voltage Δv_c is from the current sample to the next, where the voltage of the next sample should be v_c^* from Eq. (4.8) which was just computed as the necessary voltage to meet the grid reference. The current reference being dependent on the expected v_c^* means the controller should place emphasis on this state, in order to be able to meet the computed converter current reference. This should be considered in the choices of weighting in the cost function.

4.3.1 Extrapolation of Reference

Because predictions are made to the $(k+2)'th$ sample time, the references are extrapolated equally to avoid using outdated values. This is done by generic 2nd order Lagrange interpolation, for which the interpolated polynomial is given by:

$$P(x) = \frac{(x-x_2)(x-x_3)}{(x_1-x_2)(x_1-x_3)}y_1 + \frac{(x-x_1)(x-x_3)}{(x_2-x_1)(x_2-x_3)}y_2 + \frac{(x-x_1)(x-x_2)}{(x_3-x_1)(x_3-x_2)}y_3 \tag{4.10}$$

This yields the second order polynomial that passes through any three points $[x_i, y_i]$ for $i = [1,2,3]$. To show the second order nature of the polynomial the first fraction is expanded with values of i inserted:

$$\frac{(x-2)(x-3)}{(1-2)(1-3)}y_1 = \frac{1}{2}(x^2 - 5x + 6)y_1$$

The polynomial Eq. (4.10) is as such an addition of multiple second order polynomials, for which the resulting polynomial is also second order.

In the discrete case, where the extrapolated points are always the current and two previous reference values, and the point of interest is the next sample, the coefficients always compute to the same values. I.e. for the next sample $(k+1) = 4$ the extrapolation points are sample instances $(1,2,3)$ with reference values $\left(i^*(k-2), i^*(k-1), i^*(k)\right)$. Equation Eq. (4.10) then becomes:

$$
\begin{aligned}
i^*(k+1) &= \frac{(4-2)(4-3)}{(1-2)(1-3)} i^*(k-2) + \frac{(4-1)(4-3)}{(2-1)(2-3)} i^*(k-1) + \frac{(4-1)(4-2)}{(3-1)(3-2)} i^*(k) \\
&= \frac{2}{2} i^*(k-2) + \frac{3}{-1} i^*(k-1) + \frac{6}{2} i^*(k) \\
&= i^*(k-2) - 3i^*(k-1) + 3i^*(k)
\end{aligned} \tag{4.11}
$$

To compute $i^*(k+2)$ we can shift Eq. (4.11) forward, giving:

$$
i^*(k+2) = i^*(k-1) - 3i^*(k) + 3i^*(k+1) = 3i^*(k-2) - 8i^*(k-1) + 6i^*(k) \tag{4.12}
$$

As such $i^*(k+2)$ can be computed using only current and previous values.

Note that the second order extrapolation is the minimum order required to represent sinusoidal variables, and that higher orders can be considered [3].

4.4 Cost Function and Constraints

The advantage of MPC is its ability to consider a variety of objectives collected in a cost function. The simplest version only considers the error between predicted values, and reference values, which ensures reference tracking. The commonly used quadratic cost function of the tracking errors are:

$$
g_{track}(k+2) = \lambda_{track}(\mid x^*(k+2) - x^P(k+2) \mid^2) \tag{4.13}
$$

where $x = \begin{bmatrix} i_{1\alpha} & i_{1\beta} & i_{2\alpha} & i_{2\beta} & v_{c\alpha} & v_{c\beta} \end{bmatrix}^T$ and $\lambda_{track} = \begin{bmatrix} \lambda_{con_\alpha} & \lambda_{con_\beta} & \lambda_{g_\alpha} & \lambda_{g_\beta} & \lambda_{v_{c\alpha}} & \lambda_{v_{c\beta}} \end{bmatrix}$. λ_{track} makes it possible to weight which reference that is the most important to reach. This also makes the tuning of these weight really important which will be discussed in the next section.

In order to reduce the commutations, or switching, done by the converter an additional term is added to penalize the use of voltage vectors that would result in more changes of the switching state compared to last voltage vector. First the number of commutations required to use the next voltage vector, n_{sw} is computed:

$$
n_{sw}(k+2) = \mid S_{abc}(k+2) - S_{abc}(k+1) \mid \tag{4.14}
$$

where $S_{abc} = \begin{bmatrix} S_a & S_b & S_c \end{bmatrix}^T$ for the corresponding voltage vector, $\mathbf{V} = [\mathbf{V}_0 ... \mathbf{V}_7]$. This means that if the next voltage vector canditate is $\mathbf{V}_3$ and the previously used voltage vector was $\mathbf{V}_1$ then $S_{abc}(k+2) = \begin{bmatrix}0 & 1 & 0\end{bmatrix}^T$, $S_{abc}(k+1) = \begin{bmatrix}1 & 0 & 0\end{bmatrix}^T$ and $n_{sw}(k+2) = \mid 0-1 \mid + \mid 1-0 \mid + \mid 0-0 \mid = 2$

$n_{sw}(k+2)$ can then be added to the cost function from Eq. (4.13) to yield:

$$g(k+2) = \lambda_{track} \mid x^*(k+2) - x^P(k+2) \mid^2 + \lambda_{sw} n_{sw}(k+2) \tag{4.15}$$

Where λ_{sw} is the weighting factor for the nr. of switching required to use the next voltage vector. Again, the tuning of λ_{sw} will be discussed in the next section.

In order to implement the secondary objectives, of not exceeding a maximum output current of $i_{max} = 5.5kA$ and keeping the DC-link voltage within $v_{min} = 950V$ and $v_{max} = 1050V$, two hard constraints is implemented in form of two more terms added to the cost function in Eq. (4.15) yielding:

$$g(k+2) = \lambda_{track} \mid x^*(k+2) - x^P(k+2) \mid^2 + \lambda_{sw} n_{sw}(k+2) + g_{imax} + g_{DCmax} \tag{4.16}$$

where

$$g_{imax}(k+2) = \begin{cases} \infty & \text{if } i^P_{con}(k+2) > i_{max} \\ 0 & \text{if } i^P_{con}(k+2) \leq i_{max} \end{cases} \tag{4.17}$$

and

$$g_{DCmax}(k+2) = \begin{cases} \infty & \text{if } v^P_{DC}(k+2) > v_{max} \\ \infty & \text{if } v^P_{DC}(k+2) < v_{min} \\ 0 & \text{otherwise} \end{cases} \tag{4.18}$$

This will insure that voltage vectors, resulting in converter currents exceeding i_{max} and DC-link voltages violating v_{min} and v_{max}, will not be picked. Note that in practice a cost of ∞ is not feasible, therefore a very high value is used instead, in this case $1 \cdot 10^9$ is used. Since the cost for violating the constraint is not ∞, even if all the predicted values is outside the allowed limits, the FCS-MPC will chose the voltage vector witch takes the system closes to the reference.

Using the same method as in Eq. (4.17) and Eq. (4.18) other constraints could also be made, e.g. a constraint on the filter capacitor voltage if limits on this voltage is of interest.

4.4.1 Weighting Factors

The weighting factors are chosen based on the primary objective for the FCS-MPC, which is to reach the converter current reference. Therefore the weighting factors λ_{g_α}, λ_{g_β}, $\lambda_{v_{c\alpha}}$ and $\lambda_{v_{c\beta}}$ should be lower than λ_{con_α} and λ_{con_β}. Beside this, the weight on the α and β parts should be equal, since both parts determines the resulting power output as seen in

Eq. (4.3). With this in mind, the weighting factor for the reference tracking of the converter current is set to $\lambda_{con_\alpha} = \lambda_{con_\beta} = 1$ and the other weighting factors for reference tracking is set to $\lambda_{g_\alpha} = \lambda_{g_\beta} = \lambda_{v_{c\alpha}} = \lambda_{v_{c\beta}} = 0.5$.

The weighting factor on the number of commutations, λ_{sw} needs to be set considerably higher than the others in order to match the scale of those values, since the currents and voltages are in thousands and the commutations are ind single digits. Therefore a value of $\lambda_{sw} = 100$ is used.

4.5 Modulation and How FCS-MPC Avoids It

The finite set of voltage vectors available to the inverter means any arbitrary desired voltage output cannot be created directly. To accommodate any output some modulation technique is necessary, allowing arbitrary voltage output from a combination of the available voltage vectors. One convenient method considering the converter is already modelled in complex coordinates is space vector modulation (SVM), this method is also vastly used in classical control methods. The eight available voltage vectors in the $\alpha\beta$-domain yield the vectors and corresponding sectors between them shown in Fig. 4.5:

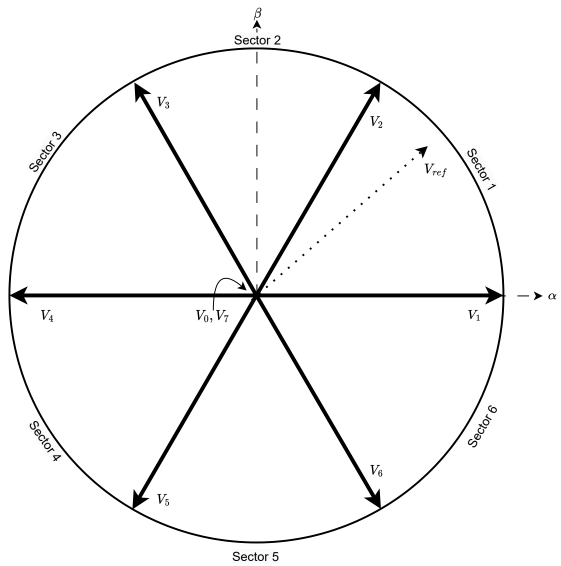

Figure 4.5: Sector Diagram

Six sectors are outlined by pairs of vectors, and an arbitrary reference vector V_{ref} is shown in sector 1. The objective is to find the sector containing V_{ref} and compute the duty cycles for the adjacent vectors, such that the combined application of both vectors approximates the reference. To find the correct sector, the predicted cost of each voltage vector is computed. The two lowest cost vectors define the sector of interest, the cost of both vector and the zero vector is then used to compute their duty cycles d according to [7]:

$$d_i = \frac{\delta}{g_i} \qquad\qquad \sum d_i = Ts \tag{4.19}$$

where i is the selection of the two vectors conforming the sector and one of the zero vectors ($V_0 = V_7$). δ is a proportionality constant, and g_i is the cost associated with each vector. Solving both equations, the proportionality constant can be found, and the duty cycles are given by:

$$d_0 = \frac{Tsg_ig_{i'}}{g_0g_i + g_ig_{i'} + g_0g_{i'}} \tag{4.20}$$

$$d_i = \frac{Tsg_0g_{i'}}{g_0g_i + g_ig_{i'} + g_0g_{i'}} \tag{4.21}$$

$$d_{i'} = \frac{Tsg_0g_i}{g_0g_i + g_ig_{i'} + g_0g_{i'}} \tag{4.22}$$

where i and i' are the first and second vector conforming the sector. The switching pattern corresponding to the selected voltage vectors can now be applied at the times specified by the duty cycles:

$$T_0 = Ts - Tsd_0 \qquad\qquad T_i = Ts - Tsd_i \qquad\qquad T_{i'} = Ts - Tsd_{i'} \tag{4.23}$$

The modulation approach can be used with MPC, but the speed of FCS-MPC allows the modulation step to be skipped. As such the controller takes the responsibility of directly making the decisions of choosing correct combinations of voltage vectors to yield the reference output on a sample by sample basis. Modulation is essentially running blindfolded for the duration between updates to the modulation function, any inaccurate prediction or disturbances in the period is not acted upon. Letting the control algorithm decide every single output vector allows it to adjust sooner. Removing modulation also allows the opportunity of reducing switching commutations, which is directly included in the cost function. Although this advantage comes at the cost of variable switching frequency, which makes filter design more difficult. The method also requires increased sampling frequency of FCS-MPC to produce the sample by sample actuations, which comes at the expense of requiring more computational power.

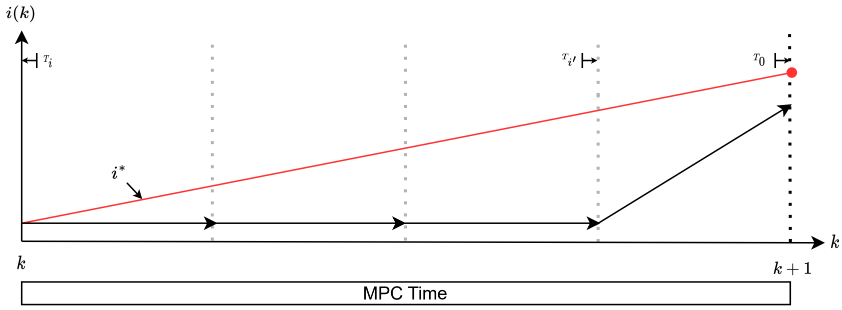

(a) FCS-MPC with a slow sampling time and modulation. Notice application times $T_0, T_i, T_{i'}$ given by Eq. (4.23), times must be matched to the discretisation, meaning the 0 vector is never actually applied.

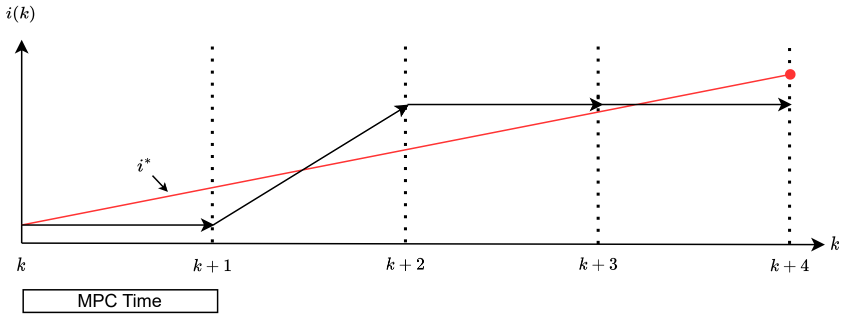

(b) FCS-MPC with fast sampling time, resulting in similar behaviour as with modulation.

Figure 4.6: Visualisation of resulting current trajectories with or without modulation.

Fig. 4.6(a) shows current trajectories with (a) or without (b) modulation for a constant reference. Notice FCS-MPC sampling time changes, in the case without modulation the sampling time is set equal to the modulation sampling time. Intuitively, there exist a trade-off between the computational burden and accuracy depending on the sampling time of the control algorithm. The reference tracking is clearly better without modulation, shown by the tracking error on samples two and three.

The figure gives the appearance that switching commutations are quite similar for both methods. Although, lets consider a reference very close to one of the voltage vectors. Then modulation would still be forced to apply the two other voltage vectors, even for just a short period, while the FCS-MPC without modulation can choose to maintain the almost perfect voltage vector for the entire period. This is even more impactful when a small tracking error is allowed if the cost of switching is greater. Note that the discretisation of the modulation figure results in the 0 vector not being applied, essentially reducing commutations for this rough discretisation. This behaviour can be replicated for any discretisation by setting a small threshold for the application times $T_0, T_i, T_{i'}$.

The model, cost function, references and their implementation nuances presented in this chapter are combined to yield the simulation results shown in Chapter 6.

Chapter 5

Simulation

This chapter will describe the technicalities of how the FCS-MPC is simulated in Simulink, using the Simscape Electrical toolbox. Exact values used in diagrams and figures does not represent the actual values used in Chapter 6. The chapter can be skipped for readers with no special interest in replicating the simulation.

5.1 FCS-MPC Simulink Setup

A overview of the simulation setup for the FCS-MPC can be seen on figure 5.1 and every block will be described in the following sections.

Plant simulation including the converter, filter, grid and current source for emulating generator output, is contained in the *Converter, LCL Filter and Grid* box. The FCS-MPC box contain controller related elements like prediction model, reference generation and cost-function. All blue boxes are auxiliary, they include declaration of variables, and performs measurements and data Manipulation. The *Constants* box contains different constant values used in the FCS-MPC model, e.g. filter values, sampling time and references. The *Weighting Factors* box contains weighting factors, and the *Data manipulation* box contains extra calculations, like power measurements and computation of Total Harmonic Distortion (THD).

5.1.1 Alpha-Beta

The *Alpha-Beta* block transforms the three phase current and voltage measurements from the abc domain to the $\alpha\beta$ domain. The expanded block can be seen on figure 5.2, here "Icon" is the output converter current, "Vc" is the filter capacitor voltage, "Vg" is the grid voltage and "Ig" is the grid current. The term "_abc" stands for abc domain and "_ab" stands for $\alpha\beta$ domain.

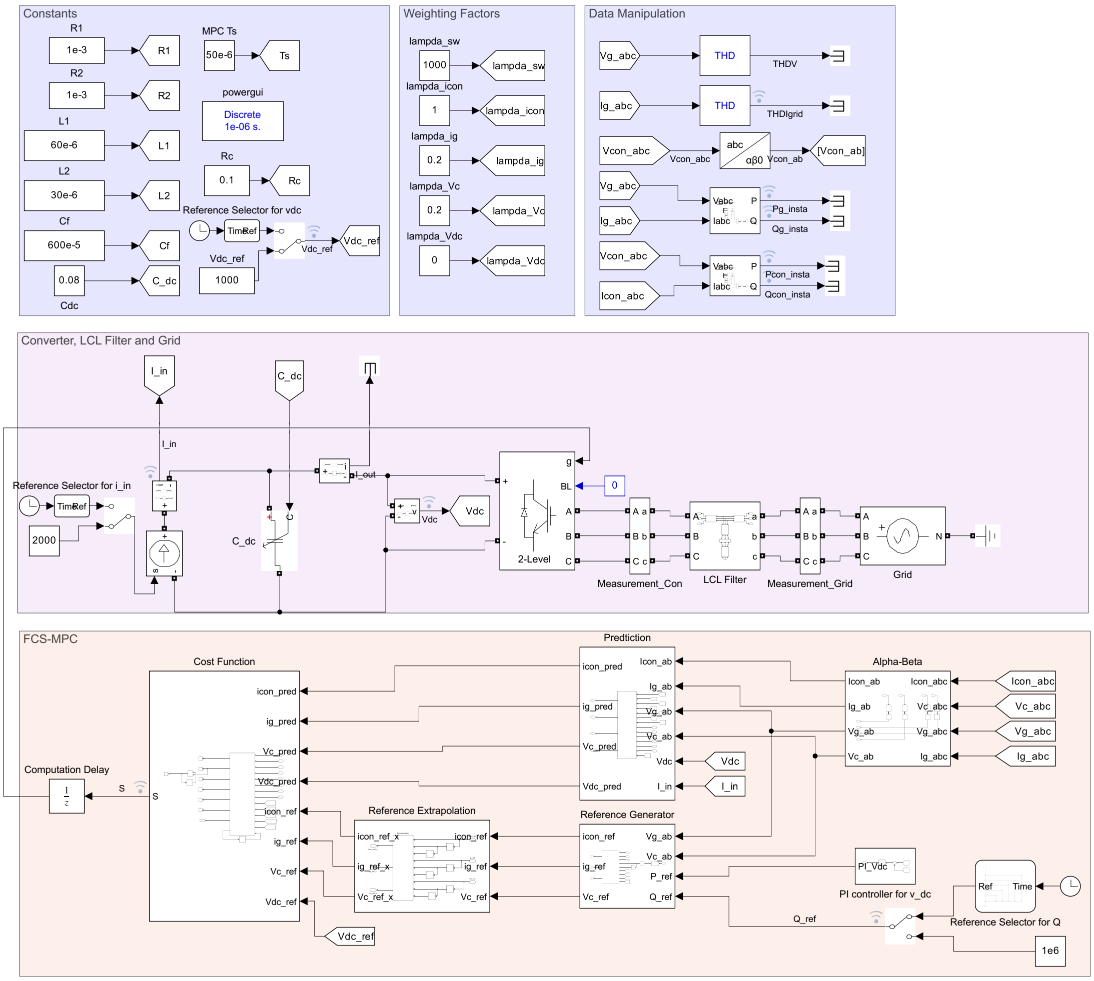

Figure 5.1: Simulation setup in Simulink.

5.1.2 References

The active power reference is given by the block *PI Controller for Vdc*, which is the PI controller, controlling the DC-link voltage ”Vdc”. If the DC link voltage rises more power has to be delivered to the grid and if the DC link voltage drops, less power should be delivered. The *PI Controller for Vdc* can be seen on figure 5.3.

The reference on the reactive power is given by either the *Reference Selector for Q* or a constant value. The *Reference Selector for Q* selects a new Q reference every 0.1 second.

The *Reference Generator* block takes the reactive and active power references, the grid voltage and filter capacitor voltage. The block then outputs the reference current for the convereter ”icon_ref”, the grid current reference ”ig_ref” and the filter capacitor voltage

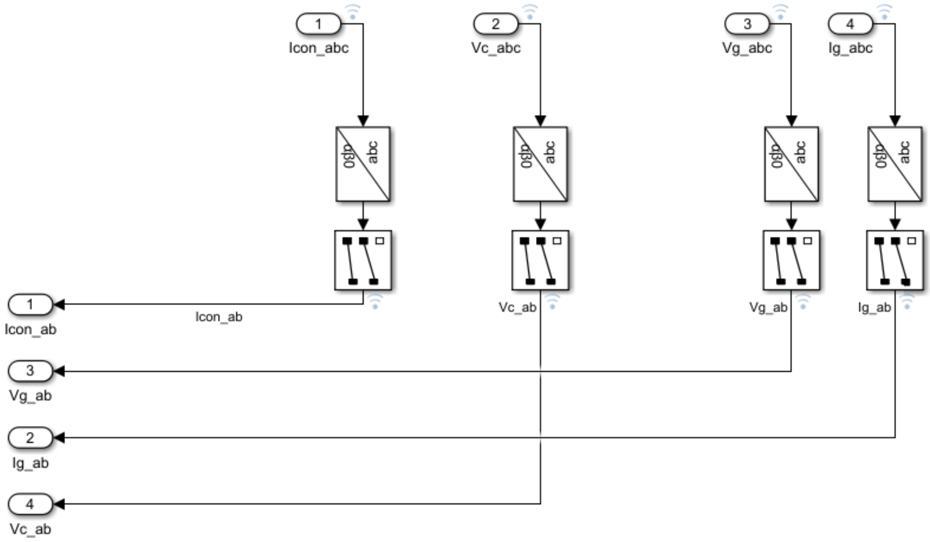

Figure 5.2: Alpha-Beta block used for transformations of measured signals.

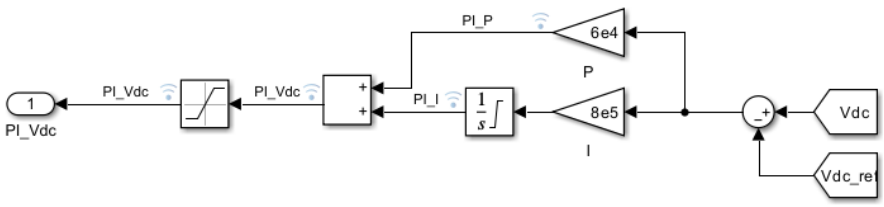

Figure 5.3: *PI Controller for Vdc* block expanded. PI controller controlling the DC link voltage by adjusting the active power reference.

reference "Vc_ref". The *Reference Generator* block can be seen on figure 5.4.

Here it is also seen that a FIR filter is used to filter the voltage measurement over the filter capacitor, "Vc_ab". the FIR filter introduces a delay, in the signal, which corresponds to a constant phase shift thereby decreasing the power factor. To take care of this phase shift, a constant offset is added, this is achieved by the 375 sample delay. This is not a viable solution to the filter delay compensation, this is further discussed in Chapter 7. An adequate FIR filter length is found to be 50 and is implemented as a moving average filter of length 50. The effect of the FIR filter can be seen on Fig. 5.5. Here it is seen that the measured filter capacitor voltage (blue) gets delayed but more smooth (red), and that the phase compensated signal is on top of the original (yellow), but one period delayed.

The *Reference Generator* block calculates the references, Fig. 5.4.

The *Reference Extrapolation* block then takes the calculated references as inputs and outputs

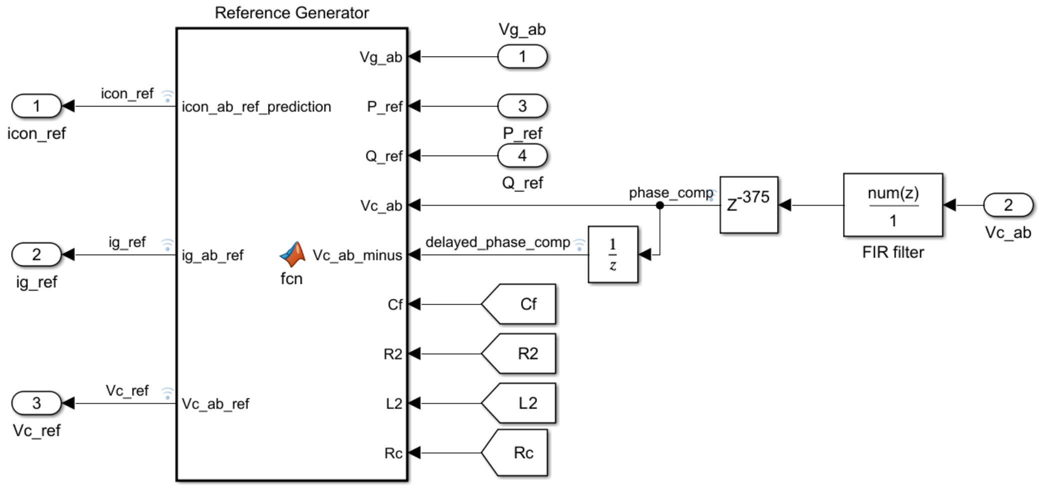

Figure 5.4: *Reference Generator* block expanded.

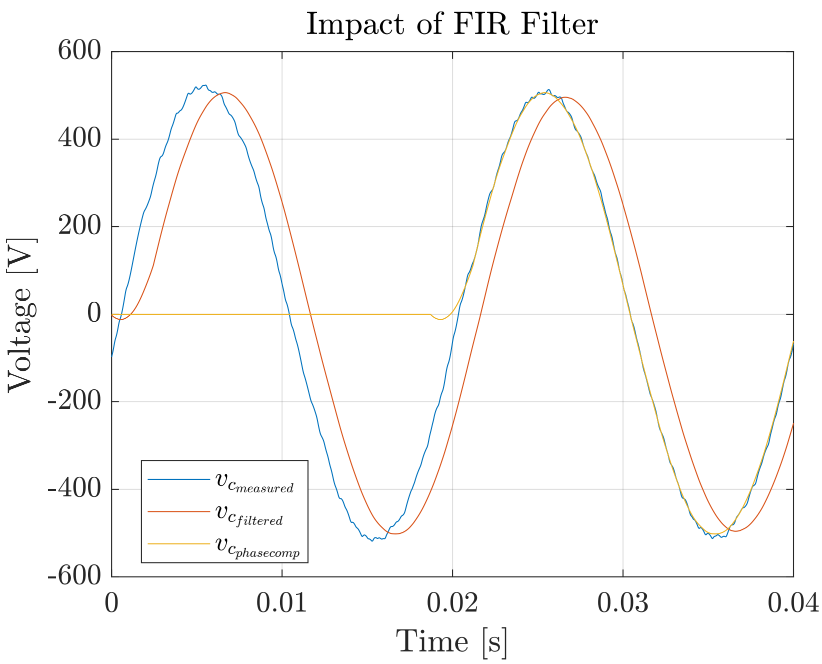

Figure 5.5: Impact of the FIR filter on the filter capacitor voltage. This shows only the α component

the same references extrapolated to the k+2 moment. The expanded block can be seen on Fig. 5.6. Unit delays are used to give the k-1 and k-2 samples, here called ”old1” and ”old2”.

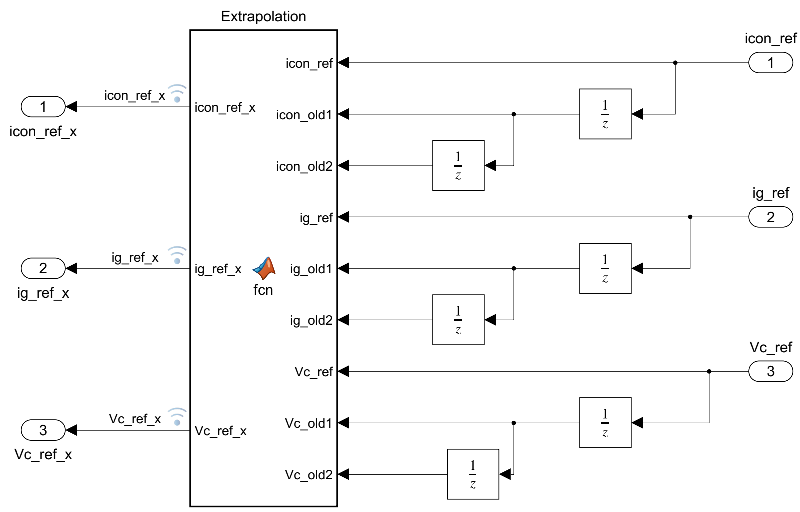

Figure 5.6: *Reference Extrapolation* block expanded

5.1.3 Prediction

The *Prediction* block on Fig. 5.1 takes all the outputs from the *Alpha-Beta* block as inputs aswell as ″i_in″ and ″Vdc″. ″i_in″ is the input current which represents the extracted wind energy from the generator side converter. The block then outputs the prediction for the current through L1, ″icon_pred″, the current though L2, ″ig_pred″ the filter capacitor voltage, ″Vc_pred″ and the DC link voltage, ″Vdc_pred″. The expanded *Prediction* block can be seen on Fig. 5.7. All the extra inputs are constants from the blue box *Constants* on Fig. 5.1.

5.1.4 Cost Function

The *Cost Function* block on Fig. 5.1 takes the outputs from the *Prediction* and *Reference Extrapolation* block as inputs, but also ″Vdc_ref″. it then outputs the optimal switching states for the converter in the form of ″S″. ″S″ is the delayed one sample, in order to

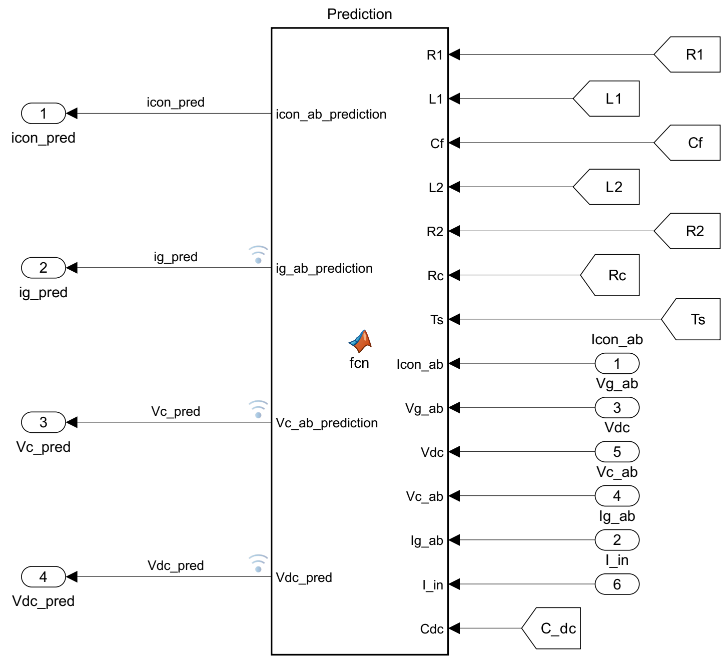

Figure 5.7: *Prediction* block expanded

simulated the computational delay from the MPC. The expanded *Cost Function* block can be seen on Fig. 5.8. The extra inputs on the figure is the weighting factors from the blue box *Weighting Factors*.

5.1.5 Converter, Filter and Grid

The converter is simulated using *Two-Level Converter* block from Simulink, with the switching device model type. The DC link of the converter is made by using a capacitor with the value of 0.08, equivalent to a capacitive reactance of 4.0 Pu [3], in parallel with a variable current source, which simulates the extracted power from the wind. Both the capacitor and the resistor are initialized in order to represent normal operation. Voltage over the capacitor is measured, and is called "Vdc". Current measurements of both the input current and output current of the DC-link is measured, called "I_in" and "I_out" respectively.

To measure the Voltage and currents of the grid and the output from the converter, mea-

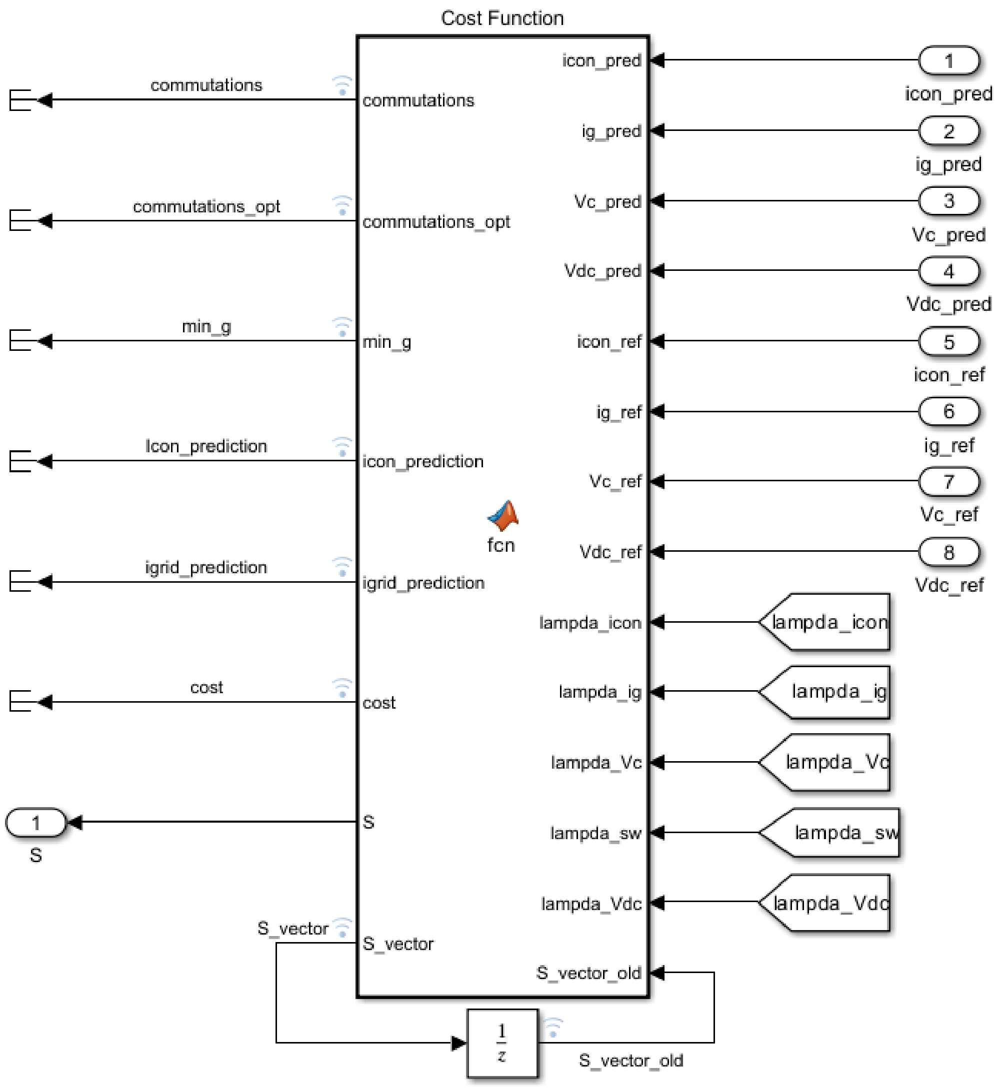

Figure 5.8: *Cost Function* block expanded

surement blocks are used on both side of the LCL filter. The LCL filter can be seen on Fig. 5.9.

The grid is simulated using the *Three-Phase Programmable Voltage Source* block, called *Grid* on the figure. The grid voltage is 630 phase-phase with a frequency of 50 Hz. A zoom in view of the converter, LCL filter and grid can be seen on Fig. 5.10.

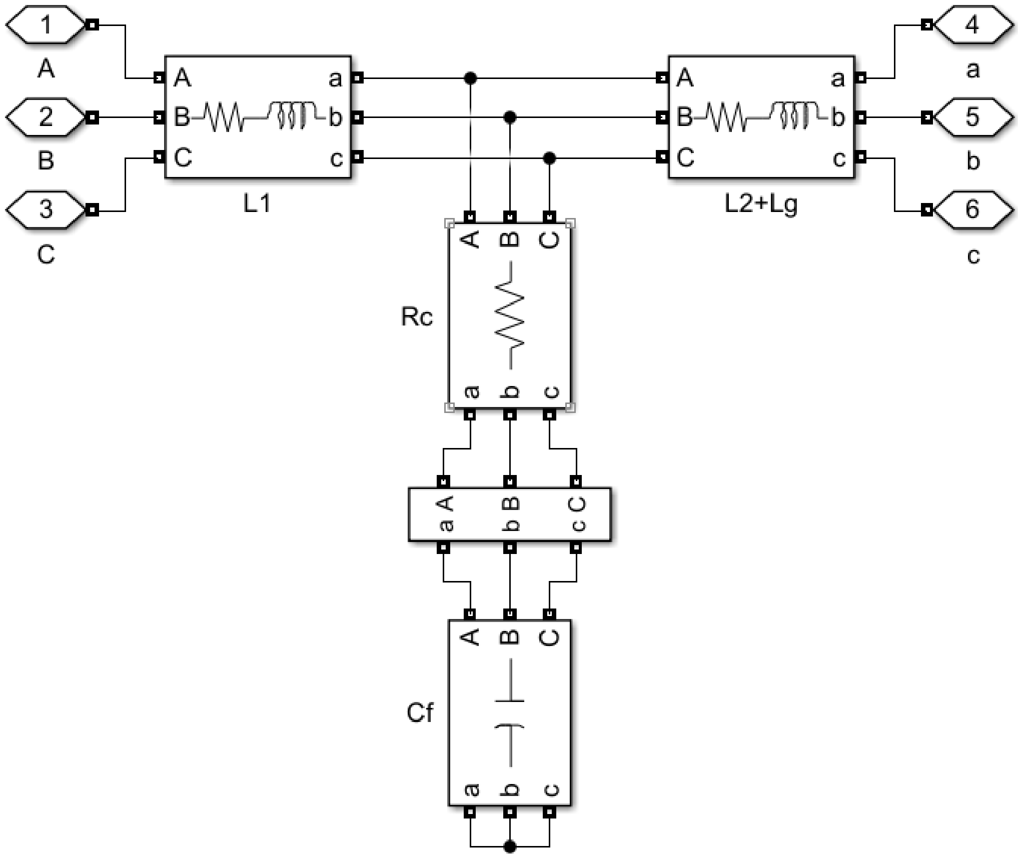

Figure 5.9: *LCL Filter* block expanded

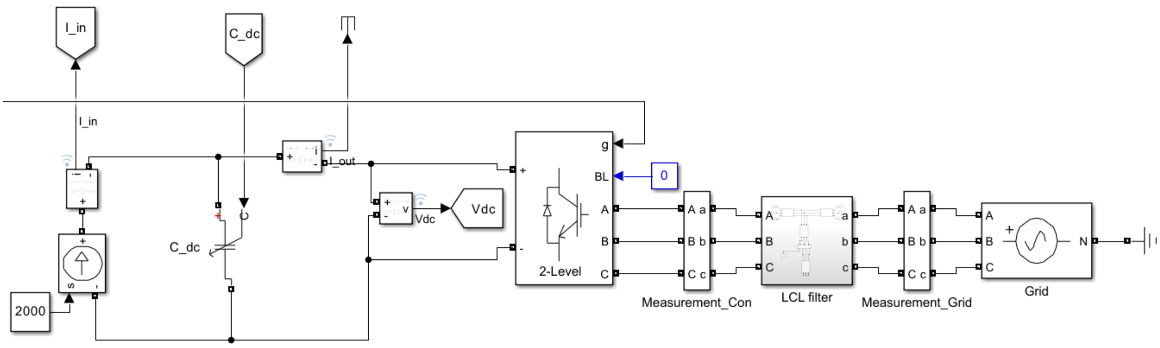

Figure 5.10: Zoomed in view of the converter, LCL filter and grid from figure 5.1

Chapter 6

Simulation Results

This chapter presents simulation results based on the simulation design described below, the more technical setup of simulation was discussed in Chapter 5. Objectives presented in Chapter 1 and a variety of other aspects are shown and commented upon. For a base of reference, a PI controller was developed as a basic foundation for performance evaluation. The choice of PI control for reference, is based on it being the current industry standard.

6.1 Simulation Design

The simulation is designed to emulate the connection of a turbine generator expressed as a current source connected to the DC-link of the converter. The connection of a three phase voltage source is used to represent the influence of a grid, and the LCL filter component values are shown below.

To reduce the amount of plots throughout this chapter, an assumption is made that α and β variables show equivalent behaviour, and therefore most simulation results are shown for α variables. Models and weights for both values are equivalent, and therefore the assumption is reasonable.

This chapter will reference two distinct PI controllers, to avoid confusion, the industry standard PI controller as a whole is denoted *PI controller*, and the PI controller for DC-link control of the FCS-MPC is denoted PI_{DC} *controller*

Simulation parameters are shown in Table 3.1 below:

Parameter		*Value*
DC-link voltage reference	v^*_{DC}	$1000V$
Converter-side inductor	L_1	$60uH$
Grid-side inductor	L_2	$30uH$
Filter capacitor	C_f	$6mF$
Internal resistance	R_1 and R_2	$1m\Omega$
Capacitor resistor	R_{cf}	0.1Ω
DC-link capacitor	C_{dc}	$0.08F$
Simulation Sample Time	Ts	$1 \cdot 10^{-6}s$
FCS-MPC Sample Time	Ts_{MPC}	$5 \cdot 10^{-5}s$
Grid frequency	F_g	$50Hz$
Grid RMS voltage phase to phase	V_{grid}	$630V$

Table 6.1: Simulation parameters.

6.2 PI Control

Currently most converter controllers are based on a classical PID approach. A set of cascaded PI controllers are used to control the currents (inner loop) and the active and reactive power (outer loop). The active power reference is combined with another PI controller in charge of maintaining the DC-link capacitor voltage, as such the active power is indirectly used to control the DC-link voltage. The dq-domain is commonly used with PI controllers, this domain is an extension of the $\alpha\beta$-domain which via an additional transformation (Park transformation) transform the oscillating $\alpha\beta$ values to static values in the dq domain, while still describing a phasor. The disadvantage is the required addition of a phase lock loop (PLL) circuit, which is an additional controller which tracks the phase of the grid. Knowing the phase of the grid at all times, allows the reference values in the dq-domain to be constant values, which is well suited for PI control. See Appendix A [2] for more information on the dq-domain.

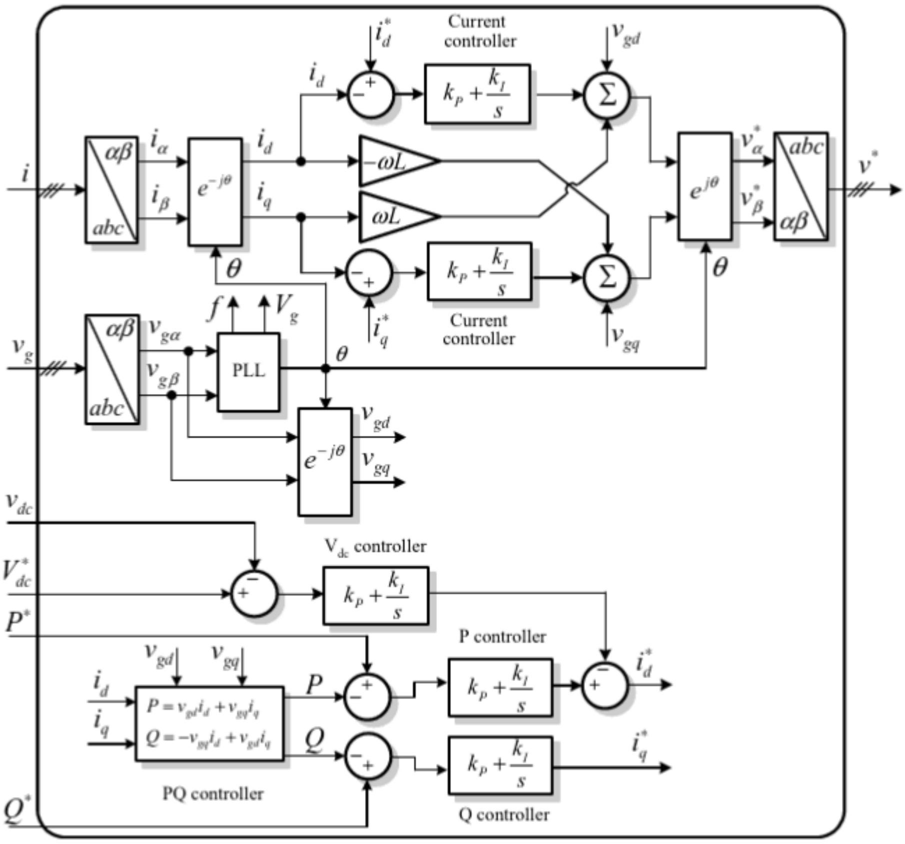

Figure 6.1: PI controller based in the dq-domain [2].

Fig. 5.3 shows the structure of the PI controller used for comparison. Notice the cascaded structure of inner loop with current controllers, and outer loop of power controllers. Noticeable features are the feed forward of grid voltage v_{gd} and v_{gq}, and cross coupling of currents which appear when the dynamics are computed in the dq-domain [2]. Remark that the P controller is unused, and the active power reference is made only based on DC-link control. For grid following purposes the active power is maximised by this approach, the inclusion of P controller is, however, potentially valuable in terms of grid forming. The use of PLL is not discussed further than what is visible in the figure, where it can be seen that the phase θ, is used in converting from $\alpha\beta$ to dq.

The following plots show the PI controllers performance for the relevant control objectives that apply to PI control, and will be used as a baseline for comparison to FCS-MPC. The modulation stage of the PI controller, was designed with a carry wave frequency that results in similar commutation as the FCS-MPC without commutation reduction.

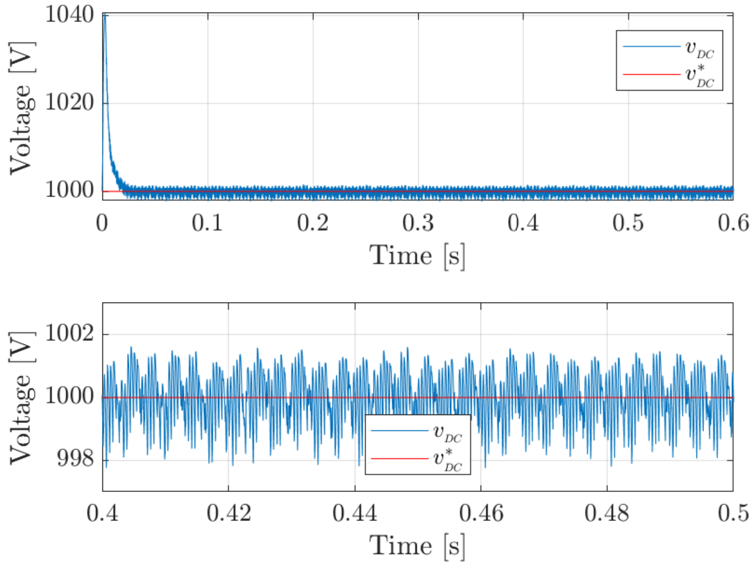

Figure 6.2: Tracking of DC-link voltage.

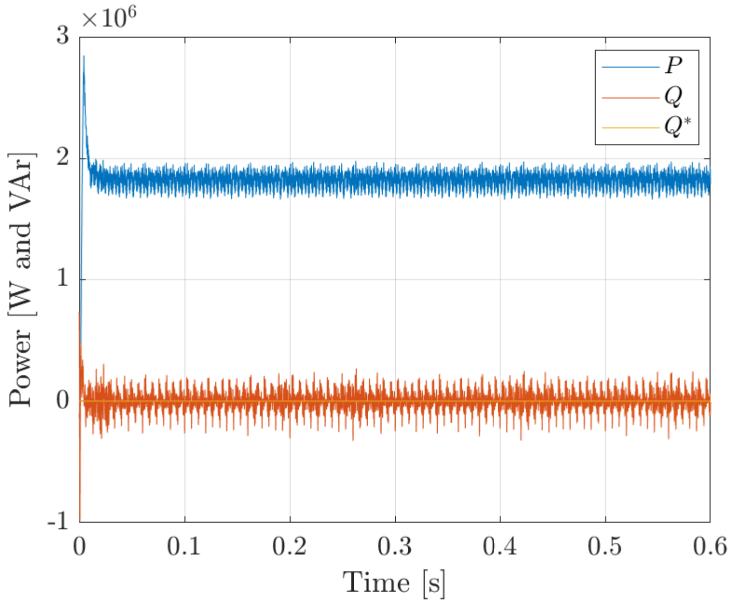

Figure 6.3: Tracking of active and reactive power. Notice there is no active power reference, since it is directly controlled based on the DC-link voltage controller.

Fig. 6.2 shows DC-link voltage, with a zoomed bottom graph to show magnitude of oscillations. v_{DC} is tracked well, with steady state oscillations of $\pm 2V$, equivalent to 0.2%.

Fig. 6.3 shows the active and reactive power tracking which are also tracked nicely with oscillations of ±0.15MW and ±0.2MW respectively.

Computing the average active- and reactive power from $t = 0.475$ to $t = 0.525$ gives $P = 1816134$ and $Q = 651$, which yield power factor:

$$Pf = \frac{P}{|S|} = \frac{P}{\sqrt{P^2 + Q^2}} = 0.9999 \tag{6.1}$$

With reactive power reference being zero, the goal of unity power factor is clearly achieved.

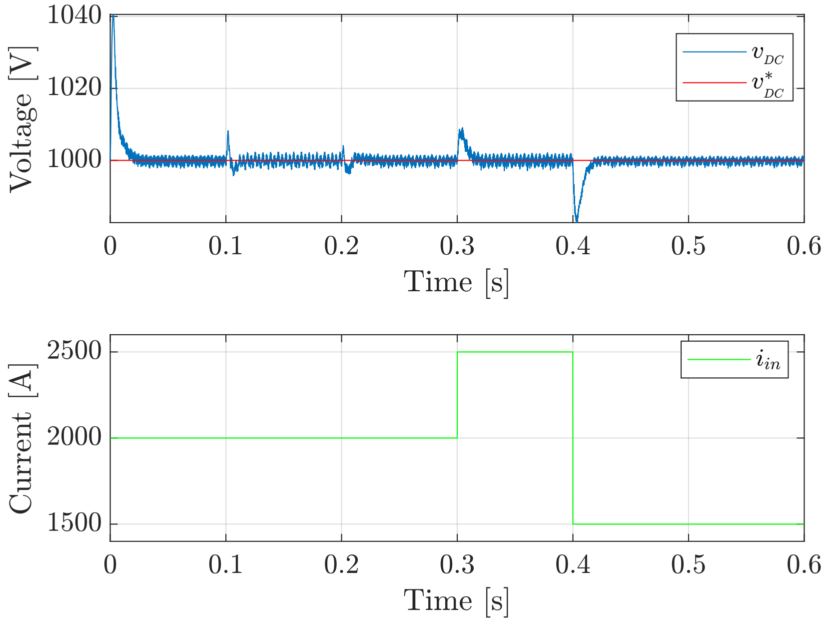

Figure 6.4: Tracking of DC-link voltage during steps in input current i_{in}, and reactive power reference. Power steps are seen in Fig. 6.5.

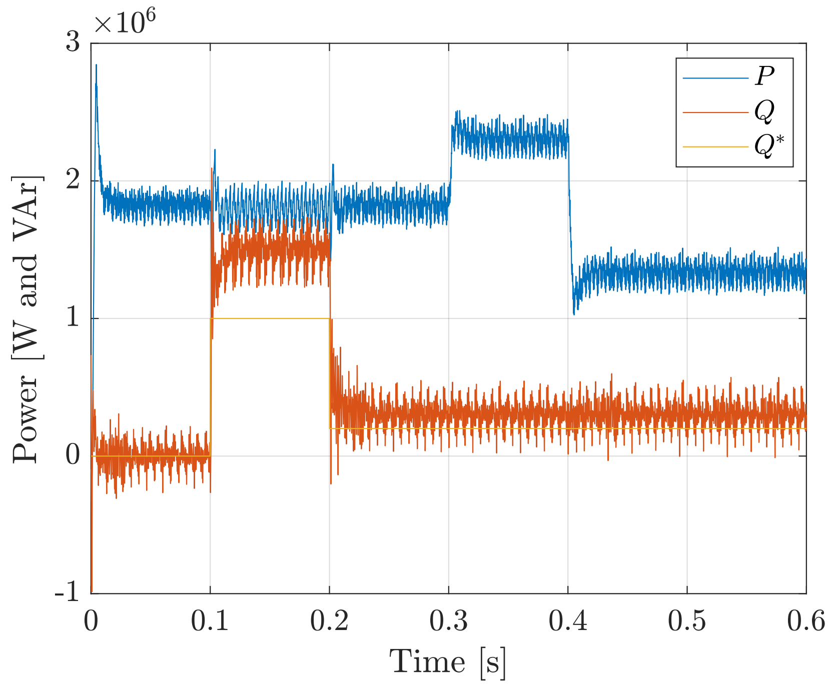

Figure 6.5: Tracking of active and reactive power, with steps in reactive power reference. Active power reference steps are made indirectly by steps in input current.

Fig. 6.4 and Fig. 6.5 shows the controllers reaction to steps in the input current i_{in} and the reactive power reference. The steps in input current are made to simulate a change of current from the generator side of the converter. Remark here, that for the PI controller, a step in input current is equivalent to a step in the active power reference since the output current i_{out} must increase or decrease to maintain the DC-link reference. For a reminder of the location of in- and output currents see Fig. 3.3. v_{DC} settles after $15ms$, and reactive power settles after $2.4ms$, similar settling time is assumed for active power, but is hard to show due to the changing reference. Fig. 6.5 shows some unexpected behaviour in its inability to reach the reactive power reference. Because the steady state error is exactly 1/3 greater than the reference for both steps, it is assumed that the power invariance property of the transformations to dq has been lost in some part of the simulation. Due to time constraints this assumed *bug* was not found.

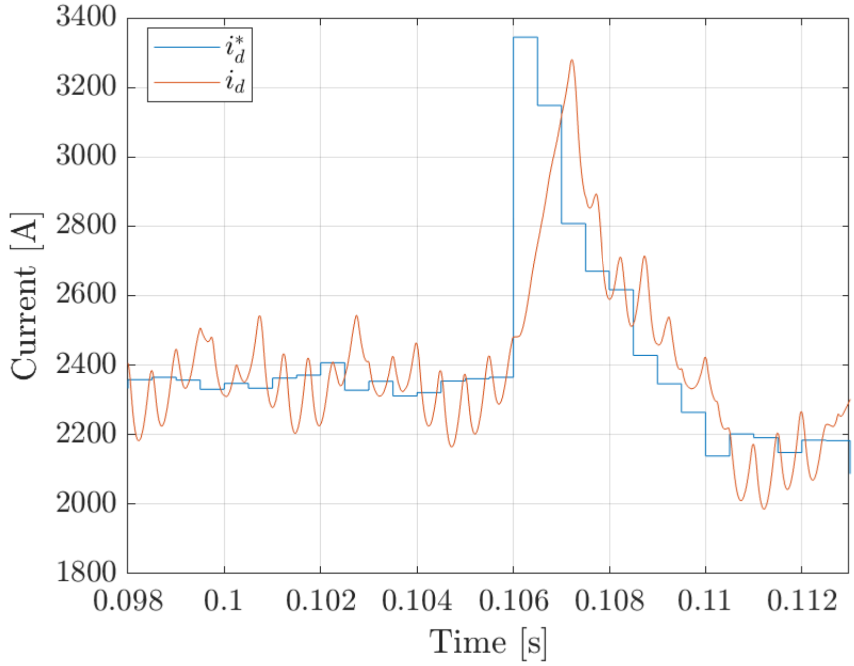

Figure 6.6: The grid current during a step in active power reference.

Fig. 6.6 shows the grid current i_d and its reference during a step in active power reference. The current is tracked nicely with a settling time of $2.2ms$ to within 10% of the reference. Its assumed that the current controller for i_q performs equivalently.

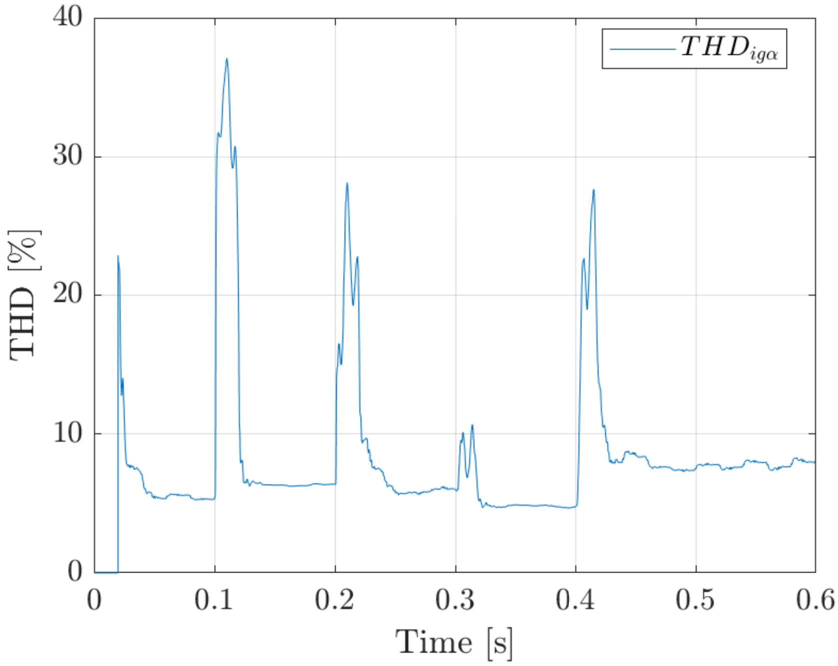

Figure 6.7: THD of grid currents using PI controller.

Fig. 6.7 show the total harmonic distortion (THD) of grid current given the same reference steps as in Fig. 6.5. THD outside of transients are around $5 - 6\%$. The spikes at power reference changes are causes because a change causes an almost immediate phase shift of the current reference which results in the perceived frequency of the wave to be altered for one period from the moment of the step. This can be seen in Fig. 6.8. As such, the spikes in THD are an artefact of the computation method, and is not representative of the actual THD, which is more accurately reflected by the steady state value between reference changes.

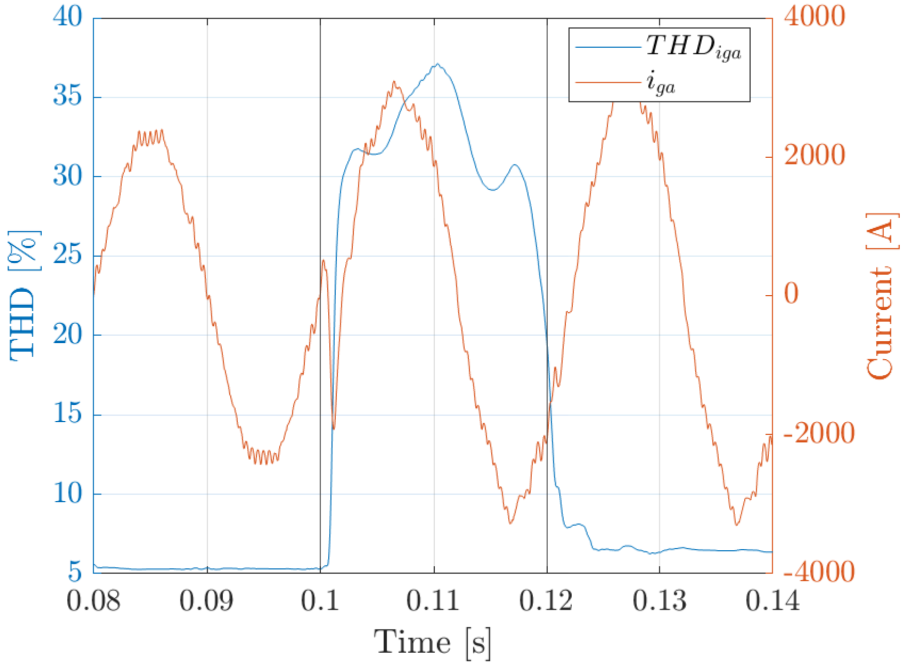

Figure 6.8: Visualisation of THD inaccuracy during the first period after a reference change.

6.3 FCS-MPC

Having made baseline benchmarks using the PI controller, the FCS-MPC scheme is now considered in terms of the same objectives. For a more detailed analysis on the FCS-MPC controller it is also considered in regards to its ability to reduce switching loses and uphold constraints. The functionality of prediction and cost function is also visualised.

Remark that the converter current reference Eq. (4.9) was not successfully implemented. For reference the equation is inserted below:

$$i^*_{con}(k) = i^*_g(k) + i_{R_C C}(k) = i^*_g(k) + C\frac{\Delta v_c}{T_s}$$

The computed values of v^*_c did not yield viable results, and therefore Δv_c is computed using the previous and the current measured voltage over it. This yields good results, but does not take into consideration the predicted v^*_c. This means the relation between grid current reference and converter current reference can be made with measurement and given references. As such the two last states of the state space are disregarded, this simplification is allowed on the basis that with high sampling frequency, the difference between measured values and predicted values is negligible. For longer prediction horizon or lower FCS-MPC sampling frequency this assumption is less valid, and the predictions should be resolved in order to expect good performance.

Proceeding with predictions of converter current only, the predicted and achieved values are shown in Fig. 6.9 to validate the model. Predictions are almost achieved perfectly, seen by the fact that the graphs almost coincide. The model is therefore accepted as a viable prediction for converter currents.

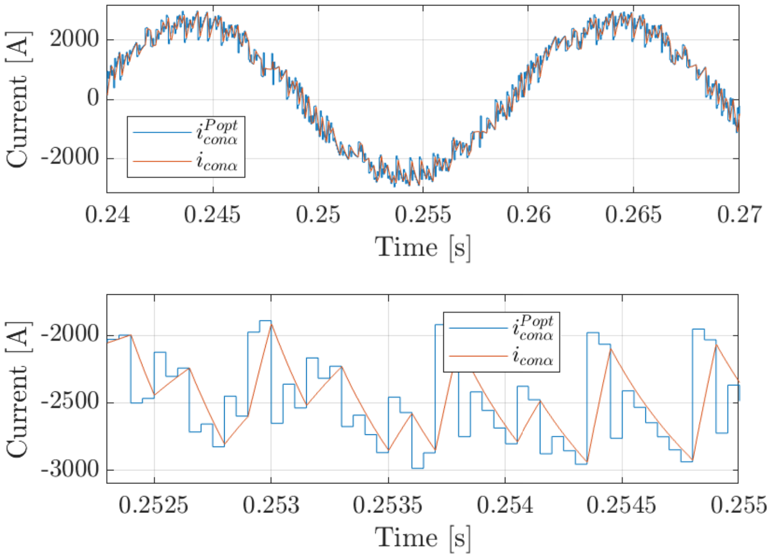

Figure 6.9: Model validation showing the optimal predicted value $i_{con\alpha}^{Popt}$ and achieved values for converter current. Bottom graph is a zoomed view.

Having validated the model, lets consider the objectives from Chapter 1, tracking of the DC-link voltage v_{DC}, reactive power and active power.

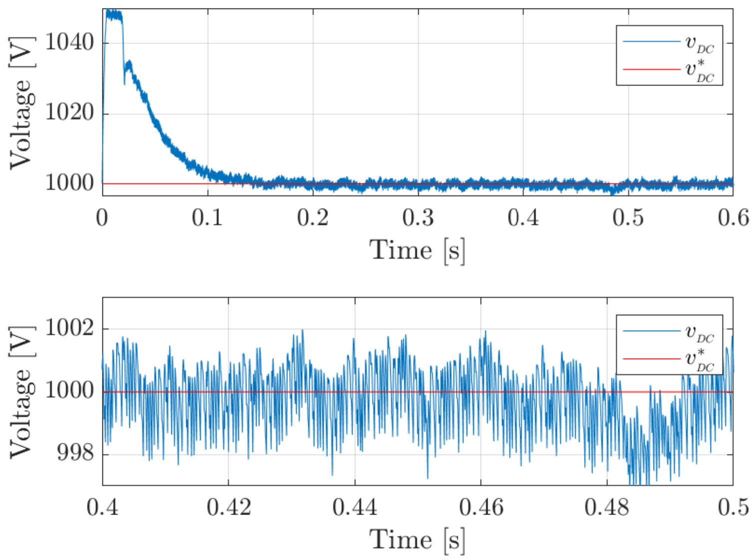

Figure 6.10: Tracking of DC-link voltage.

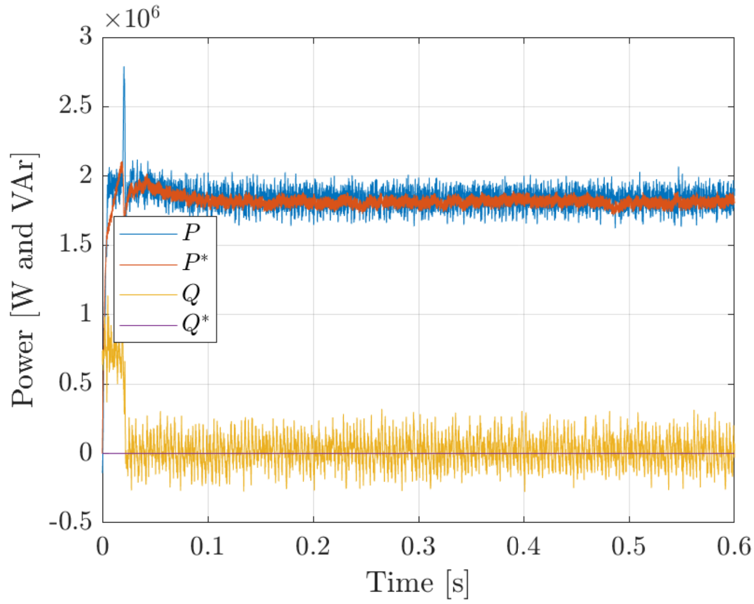

Figure 6.11: Active and reactive power tracking.

Fig. 6.10 and Fig. 6.11 shows the initial transient response. The first plot clearly shows the DC-link is successfully stabilised, and tracked nicely after settling with zero steady state error, and small oscillations of $\pm 2V$, likely caused by the discrete nature of actuations, see bottom zoomed plot Fig. 6.10. These oscillations being equally large with PI control, show no control improvement. The transient response shown here is unreliable by the excessive charging of passive components from the initial *off-state*, and the initialisation of the FIR-filter which gives a initial one period delay, further described in Chapter 7. Any other simulations results presented from here on, will be based on the period after initial transients have settled, as such the initial transients are ignored. Fig. 6.11 still make a convincing takeaway about power factor. For efficiency, a unity power factor is desired, here this correspond to zero reactive power reflected by the reference. Computing the average active- and reactive power from $t = 0.475$ to $t = 0.525$ gives $P = 1821796$ and $Q = 35961$, which yield power factor:

$$Pf = \frac{P}{|S|} = \frac{P}{\sqrt{P^2 + Q^2}} = 0.9998 \tag{6.2}$$

This power factor is slightly lower than for PI control, but still marginally close to equal one, and the objective of unity power factor is considered equally satisfied.

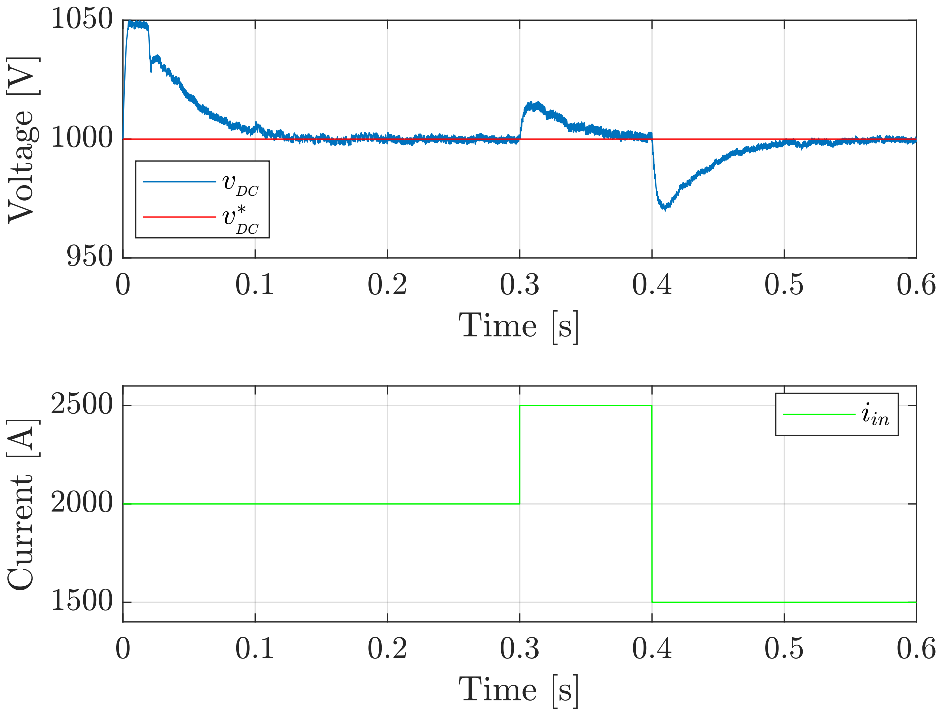

Figure 6.12: Tracking of DC-link voltage during steps in input current i_{in}, and reactive power reference. Power steps are seen in Fig. 6.13.

Fig. 6.12 shows a step in the input current to the converter. It is clearly seen that the reference is tracked adequately with settling times of 0.06s to within 10% of the reference. Settling times of the DC-link is allowed to be longer, since its down stream impact is easily handled by the MPC. The fact that the DC-link errors does not impact the other variables can be seen in Fig. 6.13, where the reactive power does not show any signs of change at $t = 0.3$.

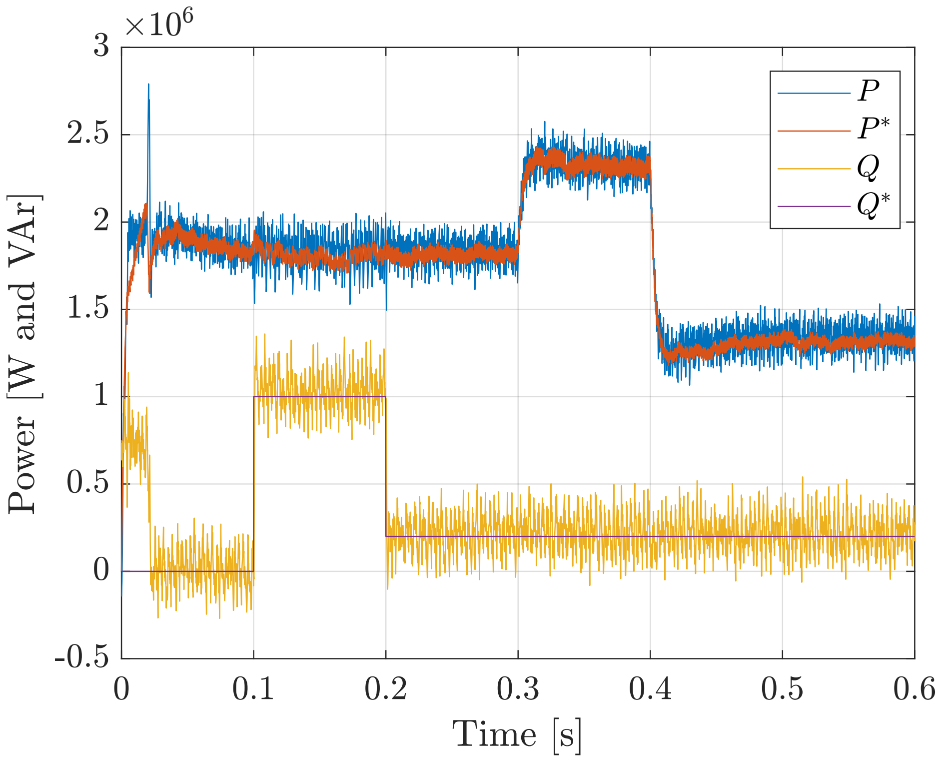

Figure 6.13: Tracking of active and reactive power, with steps in reactive power reference. Active power reference steps are made indirectly by steps in input current shown in the previous plot.

Fig. 6.13 shows a step in the active- and reactive power references. Active power reference changes are made indirectly by the same change in input current as seen in Fig. 6.12. When the input current changes and results in changes of the DC-link voltage, the active power reference is changed accordingly by the PI_{DC} controller. The active power reference is therefore changing over time with the PI_{DC} output, and it can be seen that the FCS-MPC controller is able to track the moving reference well. Assuming both power are tracked equally, the actual settling time of the power tracking is more easily seen by the discrete step in reactive power reference, with a settling time of around $1.2ms$. The moderate oscillations are caused by the fact that instantaneous power is a multiplication of current and voltage, which both are large numbers. The rms grid voltage is $360V$ for which current changes of $200A$ yield power changes of $72000W$, which is in the region of the magnitude of the oscillations. Ampere changes og this magnitude and more are clearly present in the current tracking seen in the following figures.

6.3.1 Current Prediction

The tracking of reference is an indirect result of the current tracking.

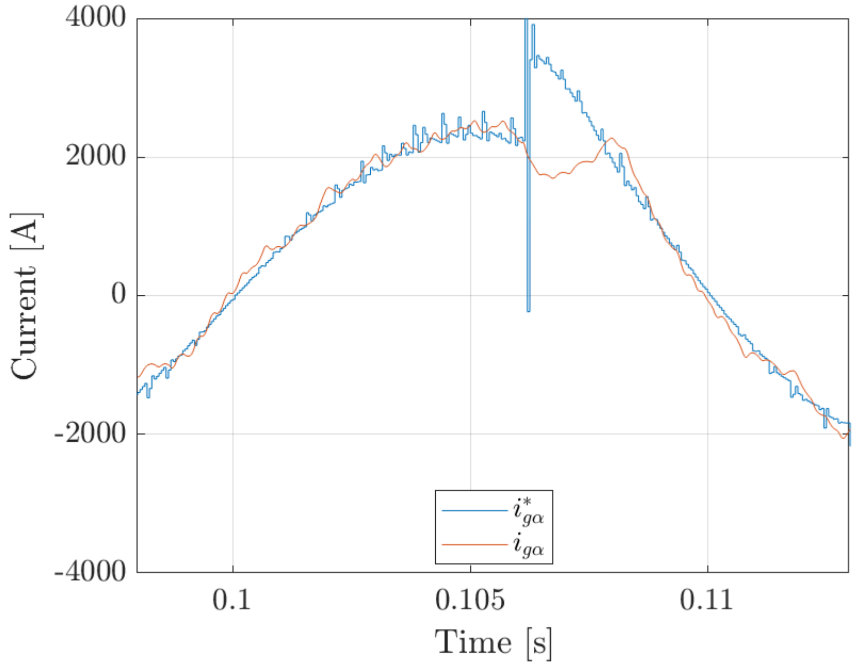

Figure 6.14: Zoomed presentation of the α grid currents trajectory and its reference during a step in active power reference.

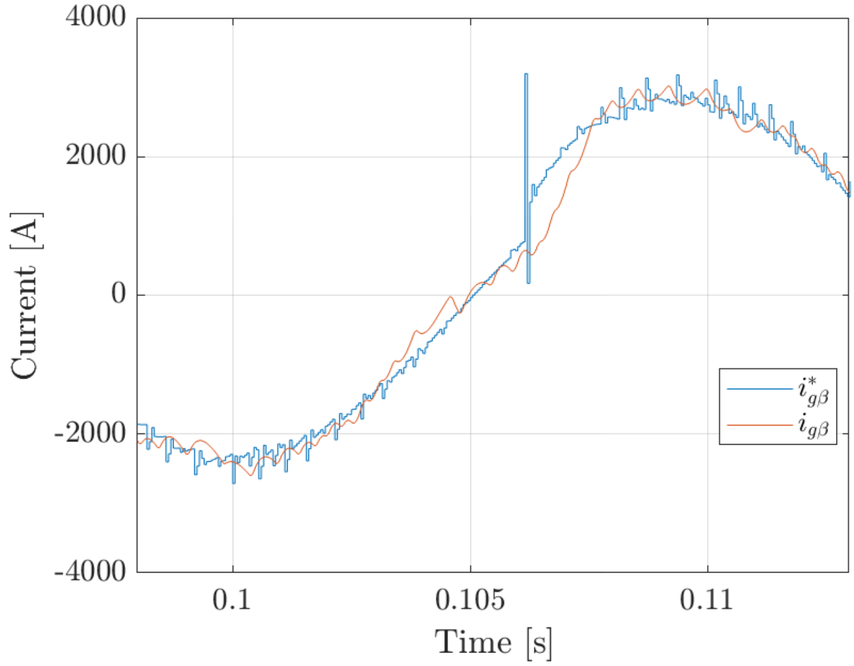

Figure 6.15: Zoomed presentation of the β grid currents trajectory and its reference during a step in active power reference.

Fig. 6.14 and Fig. 6.15 show the grid currents during a step in active power reference. Both settle at their reference after $1.2ms$, which is significantly faster than the PI controller. The spikes in reference are caused by the extrapolation which is not accurate for fast and large steps, showing one of its disadvantages. Notice that the active power reference change from the PI_{DC} controller, does not impact the current transients, because the PI_{DC} controller is much slower, as seen in Fig. 6.12.

The following plot compilation shows trajectories for all predicted current from the eight voltage vectors, along with the cost of each prediction.

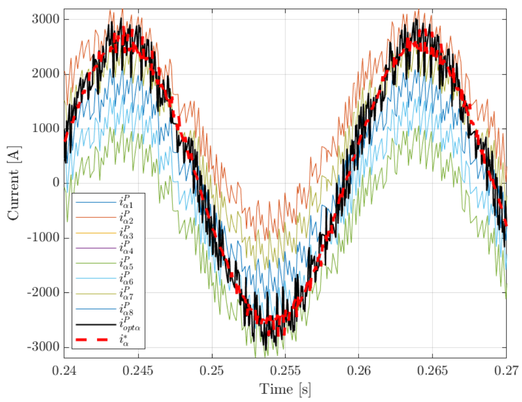

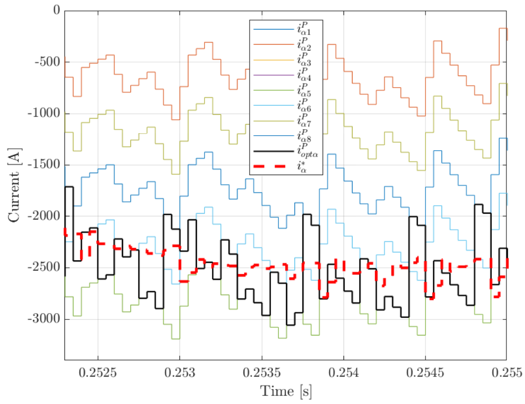

(a) Predictions of $i_{1\alpha}$, and its reference. The prediction of the optimal voltage vector is highlighted in black.

(b) Zoomed image of (a). Reference, and highlighted prediction still shown.

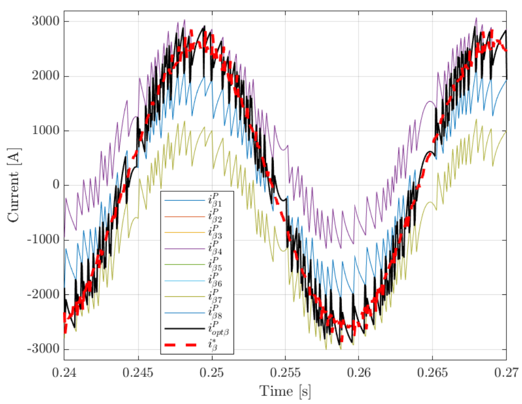

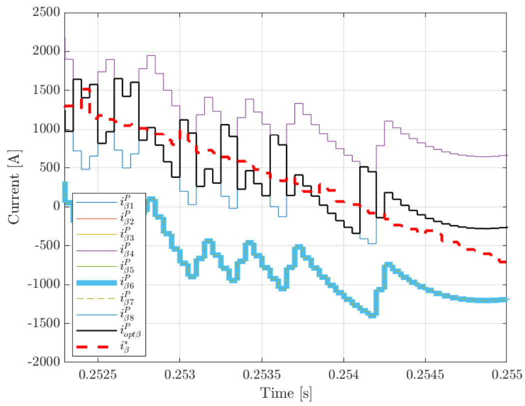

(c) Predictions of $i_{1\beta}$, and its reference. The prediction of the optimal voltage vector is highlighted in black.

(d) Zoomed image of (c). Sixth prediction highlighted in blue. Reference, and optimal prediction also included.

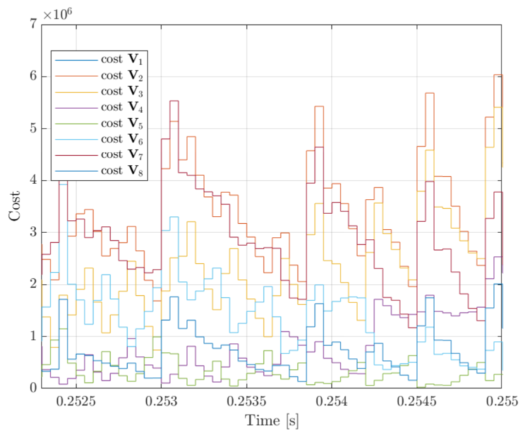

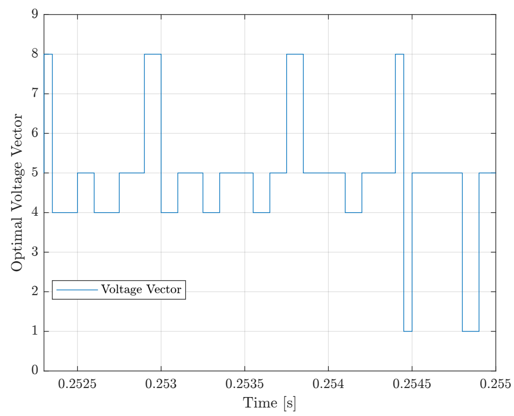

(e) Resulting cost of all voltage vectors. Notice the zoom is similar to (b) and (d).

(f) Visualisation of which voltage vector results in the lowest cost.

Figure 6.16: Compilation of plots related to converter current prediction, notice the converter subscript $(_{con})$ has been neglected to reduce legend size. Both α and β currents are shown in plots $a - d$, the right plots are zoomed images. The bottom plots (e-f) show the resulting cost of each prediction, and which optimal voltage vector is chosen based on having minimum cost.

Fig. 6.16 is a compilation of plots related to the current prediction of i_{con}. Fig. 6.16(a) shows all the $i_{con\alpha}$ predictions, the reference and the prediction of the optimal voltage vector is highlighted in black. Its clearly seen that the reference paths over the different predictions during a period, and that the highlighted black trajectory follows nicely. The black trajectory appears rough, the somewhat large discrete jumps as it oscillates around the reference are caused by the switching from one voltage vector to another. This behaviour is easily seen in Fig. 6.16(b) which shows a very zoomed in image of the same plot. Here its clearly visible that the black trajectory is confined by the discreteness of the predictions. Notice the unintuitive behaviour of *not* selecting the sixth prediction $i^P_{\alpha 6}$ as this appears closest to the reference in many cases. The cause for this is seen in Fig. 6.16(d), which shows an equivalent zoomed image of the β current. Here the sixth prediction is highlighted by a thick blue line, and its clearly seen that the voltage vector is among the worst in terms of tracking the β reference, and its total cost is therefore higher than other predictions.

Notice that due to symmetry of the voltage vectors in the $\alpha\beta$-frame Fig. 4.5, some of the predictions coincide. For α there are three pairs, resulting in five distinct trajectories as seen in Fig. 6.16(b). For β there are four pairs, of which two of the pairs have equal β value, resulting in three distinct trajectories, as seen in Fig. 6.16(d). This can result in the cost of tracking errors being equal, as seen in Fig. 6.16(e). This figure shows the cost associated with each voltage vector without considering switching losses. Notice that minimum cost is sometimes equal, resulting in an arbitrary actuation choice. This can be utilized by letting the number of commutations between switching vectors be associated a cost, reducing switching losses. Setting the weight $\lambda_{sw} > 0$, results in choosing the optimal vector by a small margin when cost are otherwise equal. This reduced switching commutations by 22%, mostly by choosing the most suited zero vector, when one of them must be chosen. The total number of commutations given different weighting values are shown in Fig. 6.17. This does not deteriorate performance in other ways, and is in essence *free*. Setting the weight $\lambda_{sw} >> 0$ reduces commutations further, but results in suboptimal choices related to tracking, this was found to increased oscillations in grid currents, beyond the allowed THD.

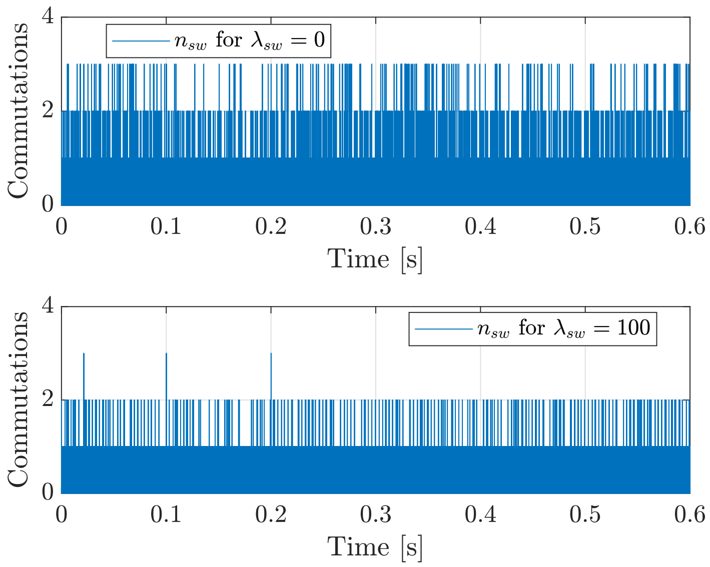

Figure 6.17: Number of total commutations over entire simulation given difference weighting factor λ_{sw}.

6.3.2 Current Frequency Content

One of the limitations of grid codes are an upper limit of THD on the grid current. The converter introduces harmonics in the produced current, these are filtered by the LCL filter.

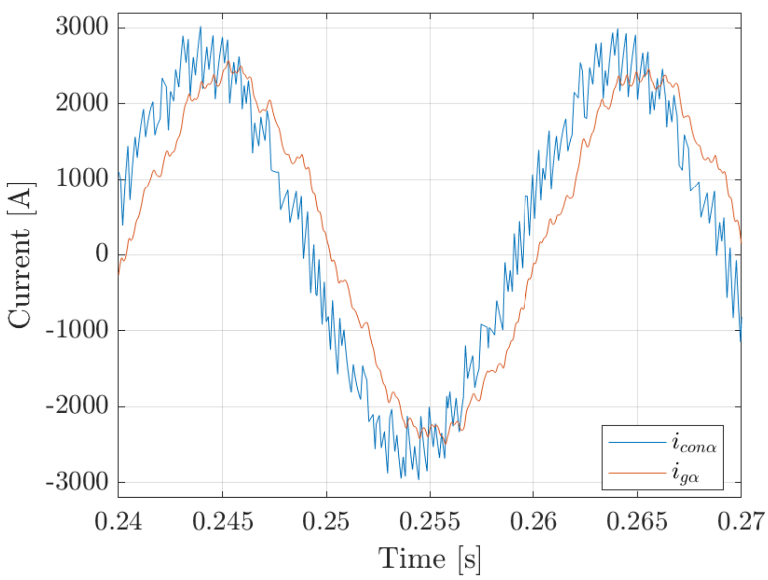

Figure 6.18: Current before and after filter.

Fig. 6.18 shows the current before and after the filter. Note two clear tendencies, the grid current is as expected much smoother, and the passive components has introduced a phase shift over the filter. To further show the filter workings the frequency content of both currents are shown in terms of THD and FFT analysis.

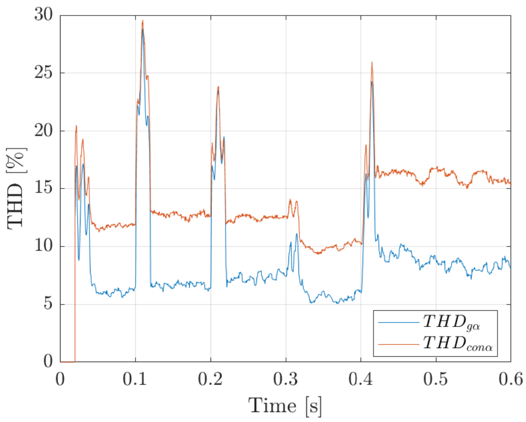

(a) Total harmonic distortion in both currents.

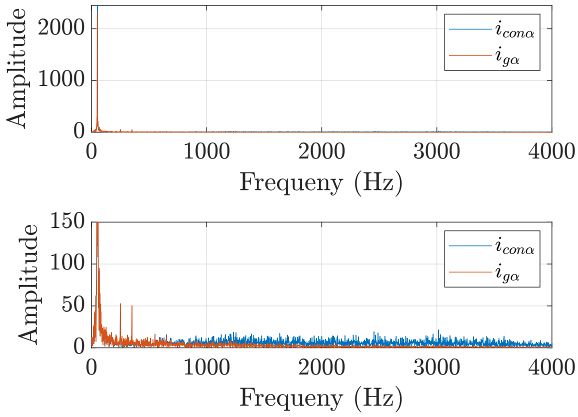

(b) FFT plot showing frequency content of both currents. Bottom is a zoomed image.

Figure 6.19: THD and FFT analysis of currents on both sides of filter. Changes of active and reactive power reference are similar to Fig. 6.13

Fig. 6.19(a) shows a clear improvement in THD, the grid distortion is about 50% better than the converter current. Notice that THD is improved in both cases when the active power reference is increased at $t = 0.3$, in both cases the increase of reference leads to an increase in current. The plot hints that the filter has improved attenuation at higher current amplitudes, and that a redesign can results in better performance.

THD is generally in the area of 5%, which is nearly within the grid codes. It is assumed that 5% can be achieved by iterating on the filter design. Fig. 6.19(b) shows the frequency content of both currents. The filter attenuation of high frequencies is clearly seen, and the fundamental frequency of $50Hz$ is dominating, with 5'th and 7'th harmonics also clearly visible.

6.3.3 Constraints

The controllers ability to avoid breaking constraints is one of its great advantages. In order to stress test the controller and check its reaction to constraints, its applied a large step in input current i_{in}, emulating a large change of current from the turbine generator.

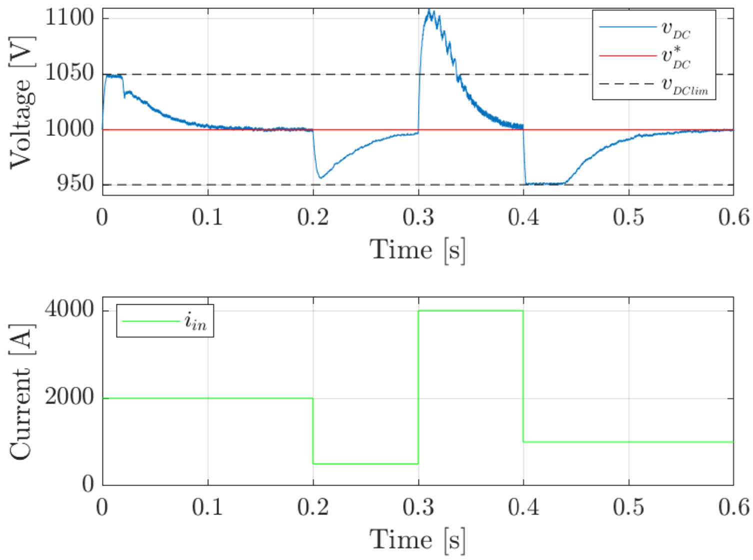

Figure 6.20: Top: DC-link voltage v_{DC}, its reference, and its constraints. **Bottom**: Steps in input current i_{in}.

Fig. 6.20 show the DC-link voltage as the input current changes are applied. At $t = 0.3$ the input step is so great that any input violates the constraint, in such a case the actuation that yield the lowest tracking cost is selected. A more appropriate approach of reducing the magnitude of the violation if its impossible to avoid by incorporating the cost of constraints as a barrier, is discussed in Chapter 7. Notice the controller does not surpass constraints at times $t = 0$ and $t = 0.4$. At the latter time step it is clearly visible in Fig. 6.21 that once v_{DC} reaches the constraint, an error in reactive power tracking begins accumulating. Similarly the approach toward the active power reference slows down. Both are results of the controller selecting voltage vectors that are suboptimal in regards of tracking, at the advantage of not violating constraints.

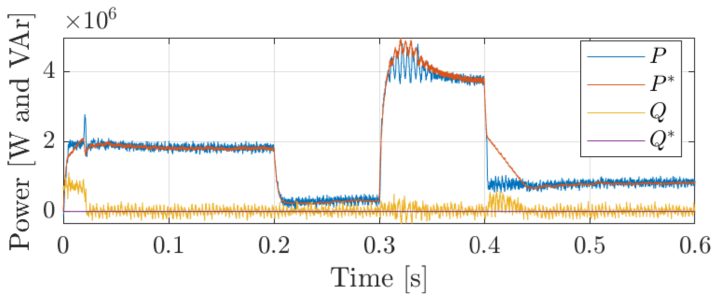

Figure 6.21: Active and reactive power, and their references during steps of i_{in}.

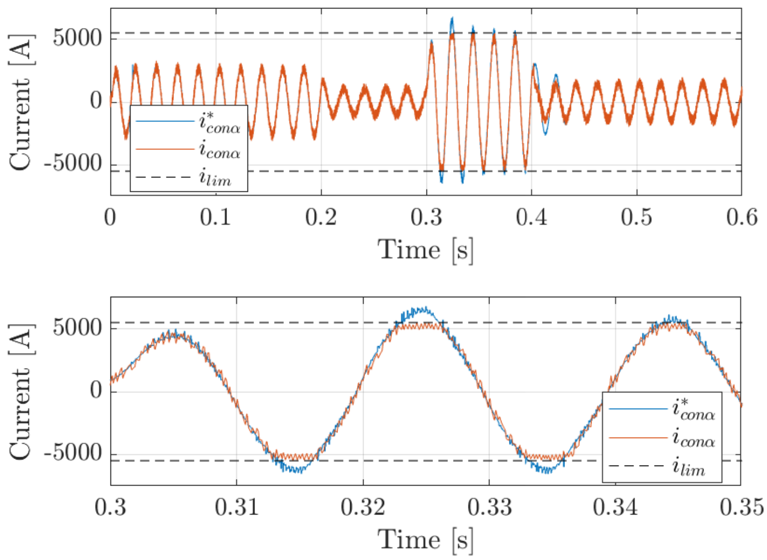

Figure 6.22: Converter currents $i_{con\alpha}$ during steps of i_{in}. Bottom graph is a zoomed image.

Fig. 6.22 shows the converter current when the steps of i_{in} is applied. Due to high constraints, violation only occurs during the very large step of input current. The peaks of this period showcased in the bottom graph, show that the converter current does not exceed its constraints. The effects of the constraint is barely noticeable, but its clear that the controller is able to respect constraints.

6.4 Comparison of FCS-MPC and PI Control

Results show the two controllers yield similar performance within multiple objectives. Both controllers are tracking the DC-link voltage reference well, with adequate settling time. The longer settling time of the FCS-MPC controller is not considered a disadvantage, since its impact is negligible in terms of power tracking and resulting THD. FCS-MPC shows settling times which are half that of the PI controller for power tracking and current tracking. The THD and power factor of both controllers are similar, which is expected although the differences in performance. This is because improved settling times are only impactful during the transient period, periods without reference changes are not impacted by the faster settling times. It is expected that higher frequency reference changes will show meaningful difference in terms of THD, duo to the transient period being longer. In essence, the faster performance is not apparent unless utilized. This hypothesis could not be validated within the time frame of this project, but is suggest for future work.

Minimization of switching losses was included in the FCS-MPC scheme with good results. The commutations was reduced by 22% with no apparent down side, because the implementation primarily yield clever selection of the zero vector. This performance was achieved for any weight above zero, further switching reduction can be achieved with a higher weight, but with a loss in THD. The choice of weighting factor for switching reduction is delicate as seen in Fig. 4.2 and 4.3 of [8]. The majority of switching reduction happens over a very short range of weighting factors. This exhaustive search was not done during this project, but the achieved reduction shows a clear proof of the opportunity with FCS-MPC.

In conclusion, the similar performance of both controllers is perceived as a success. For the reason that FCS-MPC still has untapped potential, in the form of extending horizons, active filtering, switching reduction and other secondary objectives. These, and other possible improvements are mentioned in Chapter 7.

Chapter 7

Discussion

This chapter discusses various aspects of FCS-MPC.

7.1 FSC-MPC Improvements

This section discusses improvement options realized during the project, but which was not implemented within the time scope.

7.1.1 Discretisation Strategy

The model used in this project was discretized using the forward Euler method for its simplicity. This simplicity comes with a loss of accuracy in terms of discretisation error. This yields an obvious reduction in performance and a better alternative should be considered in any real implementation. The best option as described in [3] is the exact zero order hold (ZOH) method, which yield exact discretisation in the time domain for staircase inputs, this result in significantly increased complexity of the state space model. For a simple improvement, the forward Euler method can be improved by bilinear transformation method [3]. Because the accuracy of the model is paramount to the performance of any MPC, the improvement related to discretisation could yield the last improvement in THD to meet requirements, especially using exact ZOH.

7.1.2 Barrier Function Constraint

Constraints are implemented as a hard constraint, which when broken results in a very high cost assignment. The static cost addition means that in the rare cases when all prediction break a constraint, there is no relative difference in cost between predictions in terms of their ability to return to the unconstrained area. To accommodate the fastest possible return to within constraints, a barrier cost function is suggested. The concept is to use an exponentially increasing function to assign cost to constraints instead of a static cost. The function must be designed in such a manner that the exponential increase is initialized at the constraints, the range between constraints must yield zero cost. If constraints cannot be broken under any circumstance, the beginning of the barrier can be initialized before the constraint is met, this should be especially useful for the short horizon used in this project, and result in predictions coming close to the constraint being penalised.

7.1.3 DC-link Control Directly in Cost Function

Most implementations of FCS-MPC from literature does not include control of DC-link voltage, when included a PI_{DC} controller is used by controlling active power reference based on DC-link voltage error. This is also the implementation used in this project. For the interesting aspect of being able to control the DC-link directly as an inclusion in the cost function, this was attempted. To do this, the active power reference is replaced by an approximate reference, computed by multiplying the DC-link reference voltage v^*_{DC} and the input current i_{in}. And an additional cost function term g_{DC} is added:

$$g_{DC}(k+2) = \lambda_{v_{DC}}(\mid v^*_{DC}(k+2) - v^P_{DC}(k+2) \mid^2) \tag{7.1}$$

Given steps in active- and reactive power references, as shown on Fig. 7.1, the DC-link voltage is shown on Fig. 7.2. On the figure the settling time for the DC-link voltage of $0.012s$ is very fast compared to the PI controller, which settled after $0.079s$. The fast reaction of the controller also means the magnitude of the tracking error is greatly reduced and only reaches a maximum amplitude of $5V$. It can also be seen that there is a steady state error on v_{DC}, and both power references in Fig. 7.1. compared to the results in the previous chapter. This is because the optimisation of cost has become a compromise of achieving the desired active power and maintaining an adequate DC-link voltage. Therefore the value of the weighting factor for the DC-link tracking $\lambda_{v_{DC}}$, becomes very important. It was found that $\lambda_{v_{DC}} = 1 \cdot 10^5$ gave a good compromise between DC-link voltage and active power output.

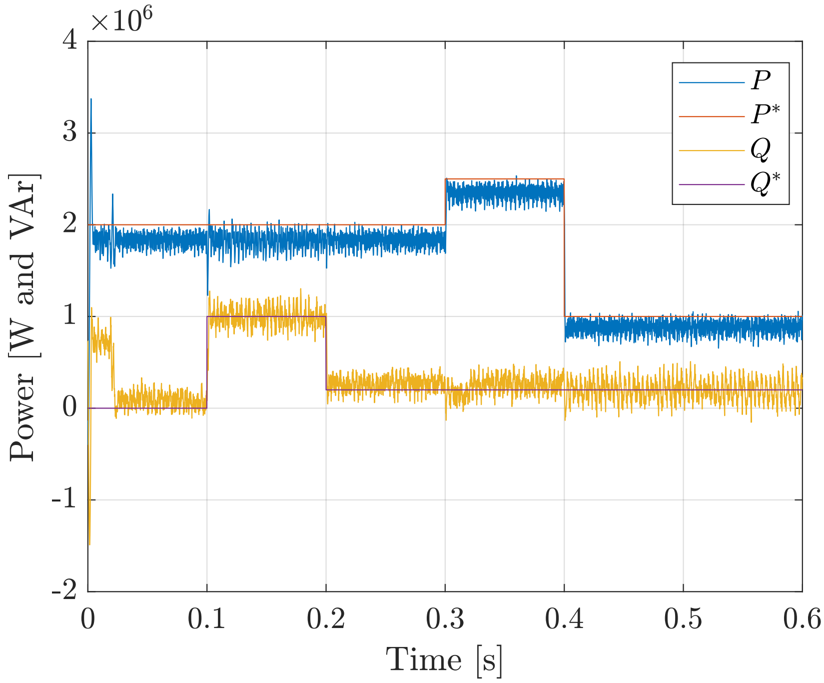

Figure 7.1: Tracking of steps in active and reactive power reference, with DC-link control included in cost function.

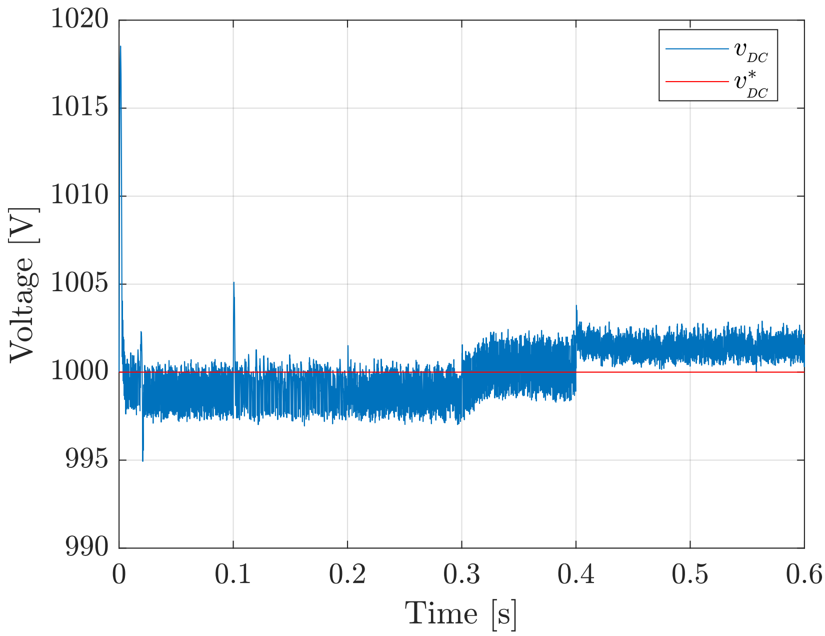

Figure 7.2: Tracking of DC-link voltage during power reference steps from above, with DC-link control included in cost function.

This compromise can also be seen on Fig. 7.1, where the active power is oscillating around a point just below the reference. It is also seen that the active- and reactive power is oscillating with approximately the same magnitude as in the original setup with the PI_{DC} controller for the DC-link voltage.

Fig. 7.3 shows THD of the grid current $i_{g\alpha}$. It is seen that the THD is around $5-6\%$ until $t=0.3$. After this, the THD is between 10% and 25% which is higher compared with the previous results. The first section, until $t=0.3$, shows the potential for this method. At this point no obvious faults can be found, and it is therefore suggested for future work to research the concept further.

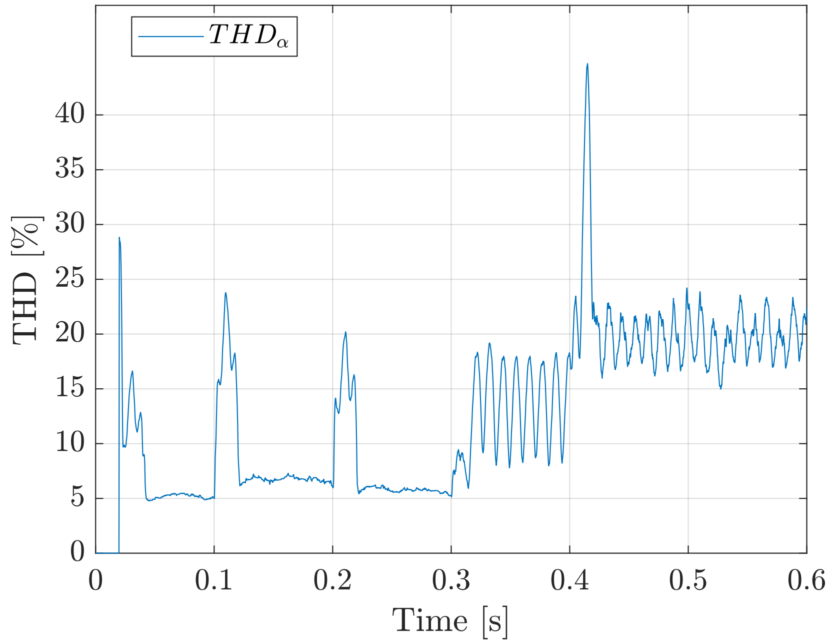

Figure 7.3: Simulation of PI controller setup in Simulink.

As a related addition, the FCS-MPC scheme could contain an element of digital filtering, with the idea of assigning a cost to predictions resulting in increases THD. This would be a complimentary cost to the increased THD caused by the tracking of DC-link voltage above. Active filtering like this is mentioned throughout literature, and can also be used in damping of filter resonance [2, 9].

7.1.4 Grid Forming and the dq-Domain

The developed FCS-MPC is operating based on the $\alpha\beta$ domain in which active- and reactive power is coupled. Therefore it is not possible to have different weights for active- and reactive power. However, if the controller is based on dq, a specific power can be prioritized, since active- and reactive power is completely decoupled. One of the important elements of modern wind turbine control is to emulate inertia on the grid, since generators with actual inertia are often related to fossil fuels [10]. The act of controlling grid properties are called grid forming, and is important in maintaining nominal values of e.g. 50Hz. This is done controlling the active- and reactive power induced into the grid, which can manipulate the grid frequency and grid amplitude. For this reason the option to weight the two independently seem advantageous, such that a specific grid fault can be targeted. The concept of grid forming is not discussed further, but is closely related to the content of this report and should be considered in further development, as the importance of grid forming increases along with the utilisation of green energy production.

7.2 FIR Filter Delay Compensation

Current references Eq. (4.9) is computed based on the measurement of the filter capacitor voltage v_c. This measurement must be filtered to avoid resonance harmonics to appear directly in the converter current reference [11]. A FIR filter is applied, see Fig. 5.5 in Chapter 5, which introduces a measurement delay. This delay is very simply compensated for by delaying the filtered output until it approximately coincide with the unfiltered measurement, this is also visualized in the figure. This filter was made without a design process and must contain room for improvement, this is especially true for the delay compensation which is very inaccurate, but was validated to have negligible impact on results by a heuristic approach. The method does however, rely on a steady fundamental frequency of 50Hz which is present in the measurement and matches the grid, as this frequency is used in computing the necessary delay for compensation. Grid faults which offset the grid frequency will skew the accuracy of the delay compensation. It is suggested for future work, that any real implementation considers a more viable solution to the filtering of capacitor voltage. If PLL is included, the extracted grid frequency can be used to compute the necessary delay online.

7.3 Extending Prediction Horizon

Most literature consider FCS-MPC implementations with short horizons, this is also the case for this project. As already mentioned, the computational burden increases drastically for longer horizons, and the optimisation approach of brute forcing the minimum value becomes infeasible. However, longer horizons has been found to yield good results [8]. By using an optimization approach called sphere decoding, a large number of sub-optimal solutions can be excluded. Although much less computational heavy, the sphere optimisation approach still only allows predictions up to a horizon of fifteen. Results show that a step in grid current reference is tracked with a settling time of $1ms$ using a horizon of 12, and $1.7ms$ using a horizon of 1. The grid current settling time of $1.2ms$ with a horizon of 2 found in the project, fits nicely in-between. Equivalent MPC sampling frequency of

20kHz is used. Further more THD was found to be 2.3% and 3.36% for the long and short horizon respectively. This clearly show the possible advantage of longer horizons, while also showing that the 5% found in this project leaves room for improvement.

7.3.1 Different Prediction Strategies and their Computation Effort

The use of sphere optimisation allow longer horizons, but the prediction strategy can also be altered to reduce the scope of optimisation. The prediction strategy with a prediction horizon of 2, and control horizon of 1 shown in Fig. 4.3, is used in this project. The prediction in [8] are made with a full control horizon, and could possibly benefit from a reduced control horizon to allow even longer prediction horizon. Although the advantage of this is not a guarantee, as the information gained from predicting far into the future can be less impactful. Another possibility is to increase the sampling frequency of the MPC while maintaining the prediction horizon, which should result in a guaranteed increase of performance. To reduce computational burden further, a strategy of simplifying the first prediction step is to only predict the actuation already chosen due to delay compensation, this is shown in [3].

7.4 Future Work

For future work this project proposes research into the utilization of longer prediction horizons, focused on exploiting the FCS-MPC ability to use the computational power available. Proper reference generation as presented in Chapter 4 should be implemented to compliment the longer horizon.

Simulation design including higher frequency reference changes should be researched to quantify the advantage of faster FCS-MPC control, especially also in regards of the inclusion of DC-link control in the cost function.

In consideration of real implementation the LCL filter design should receive greater focus than exerted in this report for its importance in reducing THD. Accordingly, active filtering by means of including frequency control in the cost function should be investigated to strive for better performance, and reduced filter cost.

Chapter 8

Conclusion

As suggested in Chapter 1 this project was based on a proposed FCS-MPC scheme for wind turbine converter control. The proposed controller has been applied and validated in terms of the listed control objectives, its performance was also compared to a PI controller subject to the same objectives, in the pursuit of finding potential advantages compared to current industry standards which use PI controllers. The performance in terms of control objectives are similar, and the results of this project does not it itself justify the advantage of the proposed FCS-MPC controller. However, the simulation design of this project does not result in full utilization of the found performance potential, in terms of shorter settling times. This is expected to be advantageous if subjected to frequent reference changes.

Another potential improvement is the flexibility in terms of exploiting the available computational effort, by increasing the prediction horizon. The performance of the short horizon FCS-MPC implemented in this project, although adequate, can be improved by extending the prediction horizon, for which strategies of prediction and optimisation discussed in this report, can be utilized to achieve a feasible computational burden.

An addition to the FCS-MPC scheme compared to most literature is the direct control of DC-link voltage, by including it in the cost function. This results in much faster DC-link tracking compared to FCS-MPC with active reference generated by a PI_{DC} controller. The performance is comparable to the industry standard PI controller, but also reduces the amplitude of the tracking error during the transient by 75%. The inclusion of DC-link voltage in the cost function can allow the FCS-MPC to sacrifice DC-link tracking for increased focus on power tracking, this is useful in terms of achieving unity power factor or grid forming.

Another advantage of the FCS-MPC cost function is its ability to assign cost to switching. Utilizing this, the total number of commutations over a simulation was reduced by 22%. The energy savings of this is not quantified, but is expected to be meaningful. However, being the sole direct improvement to PI control, the energy savings is unlikely to outweigh the aggregated workload and cost of replacing the industry standard PI controller.

The importance of grid following and grid forming control increases, with the expansion of the green energy sector. As such the ability to do this efficiently is of interest to both environmental and financial stakeholders, and there is great emphasis for companies to consider an alternative control approach which allows faster and more flexible control. The results of this project does not remedy FCS-MPC as a viable alternative at the state of implementation in this report. Its similar performance to PI does, however, suggest that FCS-MPC can be a promising method for the future, if improvements discussed in this report are fully utilized.

Bibliography

[1] Danish Energy Agency. *Danish climate policies*. URL: https://ens.dk/en/our-responsibilities/energy-climate-politics/danish-climate-policies.

[2] Remus Teodorescu, Marco Liserre, and Pedro Rodriguez. *Grid Converters for Photovoltaic and Wind Power Systems*. eng. 1. Aufl. Vol. 16. Wiley - IEEE. Hoboken: Wiley-IEEE Press, 2010. ISBN: 0470057513. DOI: 10.1002/9780470667057.

[3] Apoorva Srivastava and R. S. Bajpai. *Model Predictive Control of Grid-Connected Wind Energy Conversion System*. Vol. 68. 5. 2022, pp. 3474–3486. ISBN: 9781118988589. DOI: 10.1080/03772063.2020.1768905.

[4] Hirofumi Akagi, Edson Hirokazu Watanabe, and Mauricio Aredes. "Instantaneous Power Theory and Applications to Power Conditioning". In: *Instantaneous Power Theory and Applications to Power Conditioning* (Sept. 2006), pp. 1–379. DOI: 10.1002/0470118938.

[5] Jose Rodriguez and Patricio Cortes. "Predictive Control of Power Converters and Electrical Drives". In: *Predictive Control of Power Converters and Electrical Drives* (Mar. 2012). DOI: 10.1002/9781119941446.

[6] Hector A. Young et al. "Simple Finite-Control-Set Model Predictive Control of Grid-Forming Inverters with LCL Filters". In: *IEEE Access* 8 (2020), pp. 81246–81256. ISSN: 21693536. DOI: 10.1109/ACCESS.2020.2991396.

[7] Federico Gavilan et al. "Predictive power control strategy for a grid-connected 2L-VSI with fixed switching frequency". In: *2016 IEEE International Autumn Meeting on Power, Electronics and Computing, ROPEC 2016* Ropec (2017). DOI: 10.1109/ROPEC.2016.7830631.

[8] Joanie Michellene et al. "Model Predictive Control of a Grid-Connected Converter With LCL-Filter". In: March (2018). URL: https://scholar.sun.ac.za.

[9] Hernan Miranda et al. "Model predictive current control for high-power grid-connected converters with output LCL filter". In: *IECON Proceedings (Industrial Electronics Conference)* (2009), pp. 633–638. DOI: 10.1109/IECON.2009.5414994.

[10] Paul Denholm et al. "Inertia and the Power Grid : A Guide Without the Spin". In: *National Renewable Energy Laboratory* May (2020), p. 48. URL: https://www.nrel.gov/docs/fy20osti/73856.pdf.

[11] Chee Shen Lim et al. "Comparison of current control strategies based on FCS-MPC and D-PI-PWM control for actively damped VSCs with LCL-filters". In: *IEEE Access* 7 (2019), pp. 112410–112423. ISSN: 21693536. DOI: `10.1109/ACCESS.2019.2934185`.